

AD

**EFFECTS OF IMPACT VELOCITY AND STRESS
CONCENTRATORS IN TITANIUM ON FAILURE
BY ADIABATIC SHEARING**

Final Technical Report
(September 24/98 - November 24/99)

Principal Investigator: J.R.KLEPACZKO

**UNITED STATES ARMY EUROPEAN RESEARCH OFFICE
LONDON , UK**

CONTRACT N°: N68171-98-M-5829
R&D no: 8377 - AN - 01
Contractor:

Laboratory of Physics and Mechanics of Materials
ISGMP , UMR – CNRS 7554
METZ UNIVERSITY
F-57045 Metz, France

Approved for public release
Distribution unlimited

20000616 064

REPORT DOCUMENTATION PAGE

Form Approved
OMB No. 0704-0188

Public reporting burden for this collection of information is estimated to average 1 hour per response, including the time for reviewing instructions, searching existing data sources gathering and maintaining the data needed, and completing and reviewing the collection of information. Send comments regarding this burden estimate or any other aspect of this collection of information, including suggestions for reducing this burden, to Washington Headquarters Services, Directorate for Information Operations and Reports, 1215 Jefferson Davis Highway, Suite 1204 Arlington, VA 22202-4302, and to the Office of Management and Budget, Paperwork Reduction Project (0704-0188), Washington, DC 20503.

1. AGENCY USE ONLY (Leave Blank)	2. REPORT DATE December 1 / 1999	3. REPORT TYPE AND DATES COVERED FINAL, September 24 / 1998 – November 11 / 1999	
4. TITLE AND SUBTITLE EFFECTS OF IMPACT VELOCITY AND STRESS CONCENTRATORS IN TITANIUM ALLOYS ON FAILURE BY ADIABATIC SHEARING			5. FUNDING NUMBERS N68171-98-M-5829
6. AUTHOR(S) J.R. KLEPACZKO			
7. PERFORMING ORGANIZATION NAME(S) AND ADDRESS(ES) METZ UNIVERSITY – ISGMP LAB. OF PHYSICS AND MECHANICS OF MATERIALS ILE DU SAULCY, F-57045 METZ cedex 1, FRANCE		8. PERFORMING ORGANIZATION REPORT NUMBER N/A	
9. SPONSORING/MONITORING AGENCY NAME(S) AND ADDRESS(ES) USA RDSG-UK, AERONAUTICS AND MECHANICS BRANCH Dr. Sam SAMPATH 223 OLD MARYLEBONE RD. LONDON NW1-5TH, U.K.		10. SPONSORING/MONITORING AGENCY REPORT NUMBER N/A	
11. SUPPLEMENTARY NOTES			
12a. DISTRIBUTION/AVAILABILITY STATEMENT DISTRIBUTION UNLIMITED		12b. DISTRIBUTION CODE N/A	
13. ABSTRACT (Maximum 200 words) This Final Technical Report covers the contract period from Sept.24/1998 to Nov.11/1999. A more detailed information on the progress of this Contract can be found in the previous Interim Reports. During the period under consideration the research was directed toward effects of impact velocity and stress concentrators in titanium alloy Ti-6Al-4V on failure by adiabatic shearing. A series of experiments has been performed on Modified Double Shear specimens (MDS technique) with a square notch (standard geometry). A wide range of strain rates in shear has been applied from 10^{-4} 1/s to 10^5 1/s. The MDS specimens were loaded by a fast hydraulic machine up to strain rate 10^2 1/s and by technique of the direct impact with the maximum impact velocity 100 m/s. It has been found that the failure occurs in this alloy by adiabatic shear banding. The fracture surfaces were analyzed by Scanning Electron Microscopy (SEM). The test results were used to identify material constants in an improved constitutive relation with rate and temperature dependent flow stress. This relation was applied in the FE Code ABAQUS together with a failure criterion based on the Critical Impact Velocity in shear (CIV).			
14. SUBJECTS ITEMS ADIABATIC SHEAR BANDS, TITANIUM ALLOY Ti-6Al-4V, STRESS CONCENTRATORS IN IMPACT, DYNAMIC PLASTICITY			15. NUMBER OF PAGES 01
16. PRICE CODE			
17. SECURITY CLASSIFICATION OF REPORT UNCLASSIFIED	18. SECURITY CLASSIFICATION OF THIS PAGE UNCLASSIFIED	19. SECURITY CLASSIFICATION OF ABSTRACT UNCLASSIFIED	20. LIMITATION OF ABSTRACT

NSN 7540-01-280-5500

Standard Form 298 (Rev.2-89)
Prescribed by ANSI Std. Z39-18
298-102

EXTENDED ABSTRACT

This Extended Abstract covers the research activities on the "Effects of Impact Velocity and Stress Concentrators in Titanium on Failure by Adiabatic Shearing" carried out during the following period: from Sept.24/1998 to Nov.11/1999. Contract N° N68171-98-M-5829 granted by the ERO of the US Army (London).

During the first period of the Contract special emphasis was put on the literature survey concerning plastic behavior of Ti-6Al-4V alloy in a wide range of strain rate and temperature. Such data are important in order to properly construct an advanced constitutive relation with strain rate and temperature. It is well known that the unique experimental technique which permits for shear testing of materials within wide temperature sensitivity of plastic flow is an important factor in formation of the ASB's (Adiabatic Shear Bands). range of strain rates, typically from 10^{-4} 1/s to 10^5 1/s, that is nine decimal orders is

The LPMM has developed under previous contracts partially granted by the ERO a unique experimental technique which permits for shear testing of materials within wide range of strain rate [1]. A series of experiments has been performed on Ti-6Al-4V alloy with Modified Double Shear technique (MDS) with a square notch (standard geometry). The MDS specimens have been machined by LPMM from the plate supplied by the ARL - Aberdeen, USA. The specimens were loaded by a fast hydraulic machine with an unique system of measurements up to strain rate 10^2 1/s and by direct impact of a projectile onto specimen supported by Hopkinson tube. In the direct impact technique a complete set of measurements is possible.

The experimental results have been used to verify the constitutive relation developed in LPMM and applied previously to study the 4340 VAR steel [2]. This relation which takes into account the strain hardening, strain rate and temperature has been updated for Ti-6Al-4V, and all material constants for this alloy have been found.

Recently a failure criterion has been formulated based on adiabatic shear banding and the Critical Impact Velocity in shear [3,4]. Both, the constitutive relation and the failure criterion were introduced into the FE Code ABAQUS and the MDS technique verified.

Results obtained by this Contract are accepted for presentation during EXPLOMET 2000 and DYMAT 2000 Conferences.

CONTENTS

1. Introduction and Objectives	2
2. Technical Objectives.....	3
3. General Information on Ti-6Al-4V.....	4
4. Experiments with MDS Specimens.....	4
5. Constitutive Relations.....	7
6. Results of FE Simulations.....	8
7. FE Analysis of the Critical Impact Velocity in Shear.....	10
8. Discussion and Final Conclusions.....	13
9. References.....	15
10. Table Legends.....	17
11. Figure Captions.....	18
12. Tables 1 - 4	
13. Figures 1 - 58	

1. Introduction and Objectives

In this research program experimental and numerical studies on the effects of different impact velocities (nominal strain rates), involving the shear mode of deformation, and stress concentrators in titanium alloy Ti-6Al-4V was carried out. Since titanium is highly rate-sensitive and it exhibits relatively low rate of strain hardening, its behavior under impact loading leads to an almost instantaneous formation of Adiabatic Shear Bands (ASB). It was proposed to study the substantial differences which occur in formation and localization of the ASB's in metals, including titanium alloys, when the initial conditions, like the local stress concentrators and the local rate of shearing are extremely different.

The main purpose was to clarify, using experiments and numerical methods, the role of short-time local plastic fields with thermal coupling and the local high strain rates in development of impact failure. Some time ago a new failure criterion based on the strain energy density has been included in FE numerical code. Here, the local criterion based on the maximum strain of localization was introduced. Finally, the Modified Double Shear (MDS) experimental technique, [1,2], was used to determine characteristics of titanium within a wide range of strain rates. A fast hydraulic machine, and the direct impact technique with impact velocities from 2 m/s to 120 m/s were applied in this test program (strain rate range from 10^{-3} to 5×10^4 1/s with the MDS specimen geometry). The Critical Impact Velocity in shear was also analyzed by analytic and numerical methods. [3,4].

Mechanical tests at high strain rates as well as ballistic tests performed on pure titanium and titanium alloys, show its extreme sensitivity to formation of the ASB's, [5,6]. Consequently, studies of ASB's in titanium alloys is the most important part of the research for improvement of titanium performance against impact.

The adiabatic shear banding in metals have already been studied for some time, including experiment, analytic solutions and numerical calculations. Although some data are available as to specific critical conditions when and where the ASB's are formed, no systematic study exists in the open literature on the effect of the nominal velocities of shearing, or impact velocities, on the critical conditions for the onset and evolution of catastrophic thermoplastic shear. It may be mentioned that ASB's, with or without phase transformation, often act as the sites of fracture initiation in Mode II, [7].

Fast plastic shearing can be studied by using experimental techniques like the Split Hopkinson Torsion Bar (Kolsky torsion apparatus) or by numerical methods, including the finite differences or finite elements methods.

A few years ago an original experimental technique for fast shearing has been developed in Laboratory of Physics and Mechanics of Materials (LPMM) in Metz, [1,2]. This experimental technique is based on the Modified Double Shear (MDS) specimen geometry. The technique combines several positive features not available with other setups. The scheme of this technique is shown in Fig.5. The direct impact of a projectile is applied to deform plastically up to failure the MDS specimen shown in Fig.3. In this way the rise-time during the specimen loading has been substantially reduced ($\sim 2 \mu s$), for example in comparison to the Split Hopkinson Pressure Bar (SHPB) technique. Flat-ended projectiles of different lengths made of maraging steel and of diameter $D_p = 10.0$ mm are launched from an air gun with predetermined velocities V_0 , $1.0 \text{ m/s} < V_0 < 200 \text{ m/s}$. The impact velocity is

measured by the setup with three sources of light L , fiber optic leads 1,2,3 and three independent photodiodes F which activate two time counters $TC1$ and $TC2$. The time intervals of dark signals from the photodiodes generated during the passage of a projectile are transmitted to the start/stop gates of the time counters. The impact velocity can be precisely measured.

Axial displacement $U_x(t)$ of the central part of the MDS specimen is measured as a function of time by an optical extesometer E , acting as a non-contact displacement gage. The optical extensometer reacts to the axial movements of a small black and white target cemented to the middle part of the MDS specimen.

Axial force which is transmitted by the specimen symmetric supports attached to a long Hopkinson tube can be determined as a function of time from the transmitted longitudinal wave $\varepsilon_x(t)$ measured by SR gages T_1 cemented on the Hopkinson tube, DC supply unit A_2 and wide band amplifier A_1 . All electric signals (from the optical extensometer and SR amplifier) are recorded by digital oscilloscope DO and next stored in a PC hard disk for further analyses.

The direct impact configuration of experimental setup permits for a wide variation of the nominal strain rate in shear, typically from 10^3 1/s to 10^5 1/s. The direct determination of the axial displacement permits also for a more exact evaluation of the deformation history, a very important piece of information in development of ASB's. So far hundreds of tests have been performed with this technique, including variety of armor steels, VAR 4340 steel 50-52 HRC, aluminum alloys and shock-resistant polymers.

In conclusion, the direct impact technique available in LPMM - Metz constitutes a reliable test method to study the impact shear in the wide range of velocities.

The numerical methods, like the finite differences and the finite elements are advanced enough and they are very useful in studies of the ASB's. In addition to the finite difference method applied in LPMM-Metz to study the steady-state formation of the ASB's in 1018 steel, [8], recently, the FE method (ABAQUS implicit and explicit schemes) has been applied to study the Critical Impact Velocity (CIV) in shear, [1,2]. In this study a complete dynamic approach with the elastic-plastic wave propagation, new constitutive relation and thermal coupling has been applied to study CIV for Ti-6Al-4V alloy. The CIV in shear can be used as a new material constant, [9,10], similar to the Kàrman's critical impact velocity in tension [11,12,13]. The existence of the CIV in shear has far reaching consequences in fragmentation, [14]. The numerical study has confirmed experimental observations as to existence of the CIV in shear for 1018 steel and VAR 4340 steel 52 HRC, [2,9]. The CIV in shear causes that the energy needed to trigger an ASB is much lower when the local shearing velocity exceeds the CIV. This is a new important fact to be studied for different materials including titanium alloys. The physics of this phenomenon is now understood much better.

2. Technical Objectives

Since titanium and titanium alloys are even more sensitive to the onset of the ASB's in comparison to steels, it is of great practical interest to study, via experiment and numerical methods, the effect of stress concentrators on the triggering mechanisms of ASB's in those metallic materials. Such study could advance the state of the art in this area. A relation must be sought between titanium properties, imposed conditions in the form of different loading rates (impact velocities), stress concentrators and development of the ASB's. Also the CIV should be studied in

titanium, including experiment and numerical approach. A correlation should be sought between susceptibility to catastrophic thermoplastic shear and material properties, including CIV, including defects that initiate the localization.

The unique aspect of this research lies in application of an original and unique experimental technique developed in LPMM-Metz from one side, and an experience already gained in complete numerical analyses of the ASB's by the FE method. It is hoped that this research will have a practical significance in application to more precise design of structures against direct impact and perforation.

3. General Information on Ti-6Al-4V

Titanium and its alloys have proven to be technically superior and cost-effective materials for a wide variety of applications like aerospace, marine and armament. Titanium and its alloys are immune to corrosive attack. The key to its cost-effective use is to utilize its unique mechanical properties.

One of the most utilized titanium alloys is Ti-6Al-4V, Grade 5 alloy. This α - β alloy is the workhorse alloy of the titanium industry. The alloy is fully heat-treatable in section sizes up to ~25 mm, and can be used up to about the absolute temperature 673 K (400°C) with a small reduction of the mechanical characteristics. This alloy has specifications: DIN 3.7165 and the USA MIL-T-9047 and MIL-T-9046 AB1/2.

The mean physical data are:

1. Specific Gravity	4.43 g/cm ³
2. Melting Range	1922 +/- 15 K (1649 +/- 15°C)
3. Specific Heat	0.56 J/g K
4. Thermal Conductivity	7.20 W/m K
5. Beta Transus	1272 +/- 15 K (999 +/- 15°C)

The mean mechanical characteristics at room temperature are:

1. 0.2% Proof Stress	Min. 828 MPa ; Max. 910 MPa
2. Tensile Strength	Min. 897 MPa ; Max. 1000 MPa
3. Elongation over 50 mm	0.10
4. Reduction in Area	0.20
5. Young's Modulus	114 GPa
6. Hardness Rockwell C	36
7. Charpy Impact Energy (V-notch)	24 J

Variation of the 0.2% Proof Stress and Tensile Strength as a function of the absolute temperature, at strain rate $\sim 10^5$ 1/s, are shown in Fig 1. The temperature variation of the Elongation over 20 mm gage length is shown in Fig.2. It is clear that at temperatures higher than about 700 K the thermal softening is intensified. This information is important because the core temperature in an ASB may exceed substantially this level.

4. Experiments with MDS specimens

The experimental technique shown in Fig.5 is now a daily practice. A series of tests has been performed at room temperature on titanium alloy Ti-6Al-4V within a wide range of strain rates in shear, from 10^{-3} 1/s to $\sim 10^5$ 1/s (that is eight decimal

orders). The standard specimen geometry shown in Fig.3 was used. The specimens were machined by LPMM-Metz out of an electron beam single melt plate of thickness 25 mm. The plate designated as AR7006 was made with a special processing [15]. The chemical composition of the initial EB ingot was as follows, Wt.% (average values):

Al: 6.28; V: 4.16; O: 0.76 and other elements: Sn: 0.017-0.019; Zr: 0.022-0.024; Ni: 0.032-0.035; Mn: 0.0; Si: 0.0; Cr: 0.024-0.036; Cu: 0.001-0.004; H: 0.007-0.010; C: 0.024-0.026.

Mechanical properties:

Yield Strength	874 MPa
Tensile Strength	909 MPa

The material (titanium alloy) was delivered by ARL-WM-MC. The total number of standard specimens machined was 60. The specimens were milled in such way as to assure the shear direction perpendicular to the direction of rolling.

The main purpose of the research program was to gain more information on the effect of stress concentrators and rate effects in formation of adiabatic shear bands (ASB) and fracture.

Since there is an interest in studying not only the range of high strain rates but the whole strain rate spectrum including lower strain rates, a special device was used to load MDS specimens with a complete measurements of force and displacement, [2]. The scheme of this device is shown in Fig.4. The device is equipped with its own measuring system. The axial force $F(t)$ is measured by the load cell 6 with SR-gages and signal conditioner, and the net specimen displacements $\delta_1(t)$, $\delta_2(t)$ by two LVDT-s and two amplifiers. The MDS specimen 3 clamped to the support 2 which is loaded by the punch 4. The main support 1 with the device can be fixed to any testing machine, in this case a fast hydraulic machine was used to deform specimens from 10^{-3} 1/s to 2×10^2 1/s. The three signals from the device (force plus two displacement signals) and two electric signals from the machine can be stored in the digital form using digital oscilloscopes. The signals $F(t)$, that is the force, and LVDT' displacements are next stored in a PC hard disk for further analyses. An example of such record is given in Fig.6. From such test the shear stress and shear strain can be obtained as a function of time. After elimination of time the $\tau(\Gamma_n)$ curves can be determined, [1,2].

A series of "quasi-static" tests was performed with Ti-6Al-4V with this device and the hydraulic machine. The listing of tests is given in Table 1. The range of the shear strain rate covered is from 10^{-3} to 10 1/s. At every strain rate at least three good tests were performed. The final result in the form of the mean shear stress vs. mean shear strain is shown in Fig.7. The strain rate histories for those tests are shown in Fig.8. At higher strain rates the effect of a heat generated during plastic deformation causing thermal softening is noticeable, the point of maximum stress is shifted toward smaller shear strains.

Second series of experiments was performed with the direct impact on the Modified Double Shear (MDS) specimens, Fig.3, similar as for 4340 VAR steel, [9,16], at impact velocities $10 \text{ m/s} < V < 110 \text{ m/s}$ (nominal strain rates: $5 \times 10^{-3} < \dot{\Gamma} < 5.5 \times 10^4 \text{ 1/s}$). The complete theory of direct impact test on MDS specimen has been published elsewhere, [1]. Some oscillograms from those experiments are reproduced in figures from Fig.9 to Fig 11. The displacement signal starts earlier (movement of the black and white target on the specimen shown in Fig.5) than the signal of the

transmitted wave in the Hopkinson tube. The listing of the direct impact tests is given in Table 2. After analyses of oscillograms and elimination of time the shear stress τ vs. shear strain Γ can be determined for a particular strain rate. Such curves are shown in figures from Fig.13 to Fig.16. Because the specimens were machined "as received" (no heat treatment after milling), the scatter is quite large. However, the main trends in the behavior can be analyzed. In order to analyze the rate effect the flow stress determined at different levels of deformation can be plotted as a function of the logarithm of strain rate. Such experimental data are shown in Fig.17 and Fig.18 respectively for the low and high strain rate ranges. The level of shear strain is the "yield stress", 0.05 and 0.1 deformation level. As expected, at lower strain rates the shear flow stress is proportional to the logarithm of strain rate, Fig.17. At strain rate range from $5 \cdot 10^{-3}$ 1/s to about 10^4 1/s the measured stress increases substantially and at higher strain rates it stabilizes. Such behavior will be discussed later on. The mean values of stress are shown as black points in Fig.19. Finally, the whole rate spectrum is shown in Fig.20. The following characteristic points have also been determined from all quasi-static and dynamic tests : the maximum shear stress τ_m and the nominal strain Γ_m for this maximum, called also the instability strain, the failure shear stress τ_c and the nominal strain Γ_c at this stress (final localization strain) can also be found by an indirect method discussed later on. Experimentally determined instability strain for the lower range of strain rates is shown in Fig.21 as a function of the logarithm of strain rate. It is clear that an increase of strain rate accelerates instability and strain localization. This trend is continued up to strain rate $\sim 10^4$ 1/s, as it is shown in Fig.22 for the higher range of strain rates, and next the instability strain shows a tendency to increase. The decrease of the instability strain is due to adiabatic heating, it is leading also to an early strain localization and failure by ASB's. A more general discussion of such behavior can be found in the literature, for example [3,17]. The prediction of the instability strain based on the constitutive relation developed in the next part of this Report is shown in Fig.24.

Some specimens broken in extreme conditions, that is those loaded at low strain rate and those at very high one, were examined with the Scanning Electron Microscopy (SEM). Two lowest rates of loading at which the Ti-6Al-4V specimens were examined are $2 \cdot 10^{-6}$ m/s and $2 \cdot 10^{-5}$ m/s (nominal strain rates 10^{-3} 1/s and 10^{-2} 1/s). The SEM fractograms for those loading rates are shown in figures from Fig.25 to Fig.28. Figs.25 and 26 show quasi-brittle behavior with some cleavage patches and micro-dimples. Such behavior is partly due to an opening mode which contributed to shear fracture due to a small bending component of stress present in MDS specimen during loading just before fracture. The mean size of dimples is about few micrometers. The situation changes, however, when the loading rate is increased. At displacement rate of loading $2 \cdot 10^{-5}$ m/s, Figs.27, 28 and 29, more shear dimples are visible, together with some patches of a smeared metal where the temperature is probably already increased. At high loading rates, 98 m/s and 107 m/s, (nominal strain rates $4.9 \cdot 10^{-4}$ 1/s and $5.37 \cdot 10^{-4}$ 1/s) the smear patches are much larger, and mixed with micro-dimples, indicating for a substantial increase of the local temperature, probably close to the melting point. The size of dimples is from 1 to 10 micrometers. It is difficult to state whether the broken ASB is transformed or not since the perpendicular observation was not performed. As a whole the micro-mechanism of impact shearing in Ti-6Al-4V does not differ much from those observed in other industrial alloys, for example 4340 VAR steel [2].

5. Constitutive Relations

After careful analyses of experimental data available in the open literature for Ti-6Al-4V alloy and the results obtained with the MDS technique, the following explicit form of the constitutive relation has been worked out

$$\tau = \frac{\mu(T)}{\mu_0} \left[B \left(\frac{T}{T_0} \right)^{-\nu} (\Gamma_0 + \Gamma_p) + \left(1 - \frac{T}{D} \log \frac{\dot{\Gamma}_0}{\dot{\Gamma}} \right)^m \right] \quad (1)$$

where B , μ_0 , ν , n , m are respectively, the modulus of plasticity, the shear modulus at $T = 300$ K, the temperature index, the strain hardening exponent and the logarithmic rate sensitivity, T_0 , Γ_0 , $\dot{\Gamma}$ and D are normalization constants. This constitutive relation was used earlier to study ASB's by the FE code ABAQUS for 4340 steel [4].

The temperature change of the shear modulus in Eq.(1) is given by

$$\mu(T) = \mu_0 (1 - AT^* - CT^{*2}); T^* = T - 300 \quad (2)$$

where A and B are constants, and $T^* = T - 300$ K is the modified temperature. In principle, this version of constitutive equations can be applied at RT and temperatures above 300 K.

Since it is known that the rate of strain hardening in metals and alloys is temperature dependent and it diminishes with an increase of temperature [18]. The strain hardening exponent n was assumed as a linearly decreasing function of the homologous temperature, [18]

$$n(T) = n_0 \left(1 - \frac{T}{T_m} \right) \quad (3)$$

where n_0 is the strain hardening exponent at $T = 300$ K, and T_m is the melting point. This modification was found essential for very high strain rates.

The structure of the constitutive relation, Eq.(1), has some elements based on the materials science approach. First of all the level of stress is normalized by $\mu(T)/\mu_0$ which takes into account the thermal softening of the crystalline lattice. The first expression in the brackets is simply the internal stress and the second one is the rate and temperature-dependent effective stress, for example [8].

The procedure of how the constitutive relations have been developed is not discussed here [4]. Total number of constants in Eqs (1), (2) and (3) is 12 and they are given in Table 3. In order to better illustrate the constitutive relation used, the constitutive surface for Ti-6Al4V is presented in Fig.35 in 3D in the form of shear stress as a function of shear strain and logarithm of strain rate (upper surface), and also as a function of absolute temperature and logarithm of shear strain (lower surface).

Since a large part of the plastic work is converted into heat the temperature of a material increases when plastic deformation advances. The balance of energy with the heat conduction leads to the following relation

$$\beta\tau \frac{\partial T}{\partial t} = \rho C_v \frac{\partial T}{\partial t} - \lambda \frac{\partial^2 T}{\partial y^2} \quad (4)$$

where y is the axis of the heat conduction, β is the coefficient of energy conversion, for example [10], ρ , C_v and λ are respectively the mass density, the specific heat and the heat conductivity (Fourier constant). When the process is entirely adiabatic, $\lambda = 0$, (no heat conduction) the heating is uniform in an elementary volume. All material constants, the total is 5, are given in Table 4 of this Report. If the heat conduction is negligible an increase of temperature in the adiabatic process of plastic deformation can be calculated after integration of Eq.(4), and if the temperature sensitivity of the flow stress is already known a thermal softening of the flow stress can be finally calculated. Application of such procedures is shown in Fig.36 and Fig.37 where isothermal and adiabatic $\tau(\Gamma)$ curves are plotted for two high strain rates. Of course, thermal softening leads to the adiabatic instability and strain localization.

Thermal characteristics which are discussed above permit for numerical simulations of all temperature-coupled problems as purely adiabatic as well as with the heat conduction. The code ABAQUS includes those thermal-coupling problems in FE procedures.

6. Results of the FE Simulations

This part of the Report presents the final results obtained from the ABAQUS simulations. The final results reported here were obtained with the ABAQUS explicit FE code, [19,20]. Fig.38 shows the mesh applied and defines positions of the analyzed cross-sections of the layer, called A,B and C. The following definitions of different parameters or variables are used in the figures which show the numerical results :

- (i) Nominal shear strain Γ_n , $\Gamma_n = \Delta x_A / h_s$, where Δx_A is the displacement of the top surface (at $y = 0$), and h_s is the height of the layer, $h_s = 2.0$ mm ;
- (ii) Plastic shear strain Γ_A is the current shear strain determined in the cross-section A ;
- (iii) Plastic shear strain Γ_B is the current shear strain determined in the cross-section B ;
- (iv) Critical nominal shear strain Γ_{nc} is the strain which corresponds to the condition $\partial T_A / \partial \Gamma_n = 0$ (maximum stress) and can be determined from the $\tau_A(\Gamma_n)$ curve ;
- (v) Shear stress τ_A determined in the cross section A (at $y = 0$), this quantity is found from experiments with the MDS geometry.

The complete series of calculations was focused on analyses of the instability point as determined by $\partial \tau_A / \partial \Gamma = 0$ and conditions of localization. The main parameter in those calculations was the imposed velocity V_i .

The constants were fitted to model Ti-6Al-4V alloy. The isotropic Huber-Mises flow rule has been assumed in calculations. Because only relatively high impact velocities were analyzed the problem was treated as purely adiabatic, that is no heat exchange between elements. The state of plan strain of the mesh was assumed in all calculations. Previous Finite Elements (FE) calculations for the MDS specimen reported in [1] have shown existence of the stress concentrators around the corners of the shear zone present in the standard geometry. At high nominal strain rates those

stress concentrators trigger shear fracture by ASB's. This can be observed in Fig.19 as a stabilization of the critical stress (nominal value) at the level of ~850 MPa for strain rate higher than 10^4 1/s.

The study of the existing stress concentrators, and theirs role as a trigger of adiabatic failure was one of the objectives of this numerical analyses.

The second specific objective involving a more realistic initial conditions imposed during experiments on the MDS specimen, was to clarify the effects of plastic waves, more specifically existence of the Critical Impact Velocity (CIV) in shear [3, 4, 9].

At high nominal strain rates, as it is mentioned above, the plasticity in the shear zone is substantially reduced and a quasi-brittle behavior dominates (Fig.19). Of course, this is caused by adiabatic coupling and stress concentrators around the corners of the standard MDS geometry, [1]. This behavior indicates that the specimens of the Ti-6Al-4V tested at very high nominal strain rates, higher than 10^4 1/s, are overall "more brittle" in comparison to the tests performed at lower nominal strain rates. In order to calculate numerically an evolution of the plastic zones in the stress concentrators it is necessary to introduce a *local failure criterion*. A local criterion can be used with or without fracture mechanics principles (stress intensity factor or J-integral). In the present study a more simple approach was adapted, that is a specific value of the localization strain. This value can be determined as proportional to the instability strain defined by $(\partial\tau/\partial\Gamma) = 0$ in the adiabatic conditions of deformation with the proportionality coefficient α . Thus the local failure criterion adapted in this study is

$$\Gamma_1 = \alpha \Gamma_i \quad (5)$$

where Γ_i and Γ_1 are respectively the instability strain and the final localization strain. The instability strain was calculated using the constitutive relation introduced in the previous part of this Report and the adiabatic $\tau(\Gamma)$ curves as those shown in Fig.36 and Fig.37. The result is shown in Fig.39. In Fig.24 the instability strain estimated from experiments is slightly larger with $\alpha \approx 3.0$. The value of α for the final localization has been found by an inversion method. The nominal shear stress vs. the nominal shear strain have been analyzed numerically for seven different values of α as it is shown in Fig.40. The nominal stress was calculated via the reaction of the specimen support (Hopkinson tube) as a function of time. The nominal strain was defined as Vt/h , where V is the imposed impact velocity and h the height of the shear zone, $h = 2.0$ mm. After elimination of time the curves of Fig.40 were found and compared with the experimental curve of Fig.16. The stress maximum from experiment was close to the numerical stress maximum obtained for $\alpha \approx 50$ and this value was introduced into the local failure criterion, Eq.(5). The final localization strain is plotted in Fig.39 as a function of the normalized logarithm of strain rate with the normalized strain rate 1.0 1/s. For example, for strain rate 10^4 1/s the final localization strain is ~ 1.2 , and at this level of shear strain the elements are eliminated and shear failure propagates with a high velocity. For example, in Fig.41 are shown reconstituted curves of the nominal shear stress vs. time at two high impact velocities, 100 m/s and 140 m/s. In every case the beginning and end of the shear failure is indicated by the circular points. At 140 m/s the failure is triggered instantly and a complete failure occurs after $1.5 \mu s$, a similar value is obtained for the impact velocity 100 m/s. It is important to note that the level of the maximum stress is in agreement with experiment.

A more detailed 2D analysis how the stress concentrators are developed for the impact velocity 20 m/s (strain rate 10^4 1/s) is shown in Figs.42, 43, 44 and 45. At this nominal strain rate the overall behavior is similar to "quasi-static" one. The stress concentrations are spotted in all four corners, $t = 7.5 \mu s$, next the field of the shear deformation is close to the uniform one, $t = 15 \mu s$ and $22.5 \mu s$. Finally, a adiabatic shear band is fully developed at $t = 30.0 \mu s$.

A completely different situation is found for the impact velocity 100 m/s. Practically only one stress concentrator is activated from where the adiabatic shear band starts to propagate, this is shown in Figs.46, 47, 48 and 49. The propagation starts from the side where the impact velocity was applied, and the velocity of shear band propagation can be estimated as $\sim 1.0 \text{ mm}/\mu s$. Such behavior is called the Critical Impact Velocity in shear (CIV), [3,4,10]. The CIV in shear is a new material constant which can characterize materials in respect to fragmentation and perforation.

7. FE Analysis of the Critical Impact Velocity in Shear

A Fundamental study has been undertaken to analyze numerically the main factors which trigger the Critical Impact Velocity (CIV) in shear. The study is focussed on Ti-6Al-4V which exhibits limited rate of strain hardening at high strain rates. Occurrence of the CIV in shear for this alloy has been confirmed numerically in Figs. 46, 47, 48 and 49. In order to provide complete information on instability and localization processes when the initial boundary conditions are more realistic (closer to experimental arrangement), it was decided to define precisely how the velocity is imposed at the beginning of the shearing. Thus, to assure occurrence of strain gradients and instabilities caused by inertia, the elastic-plastic wave propagation in shear and in adiabatic conditions has been accounted for in the FE analysis.

Finally, the geometry of an infinite layer was assumed, the same as previously studied [4, 8]. The layer had a sinusoidal thickness imperfection of geometry equal to 1% along the height $h_s = 2.0 \text{ mm}$. The height is exactly the same as in the MDS geometry.

A very detailed description of the previous projects concerning numerical analyses of the infinite layer is given elsewhere [9]. Here only the main results are provided for Ti-6Al-4V.

The principal parameter in this study is the imposed velocity V_i at $y=0$. The velocity V_i was increased by 14 steps from 10 m/s up to 200 m/s. The shear velocity $V_i(t)$ at $y=0$ was applied in the specific way from value of zero to maximum V_{im} . The total rise-time t_m was chosen according to the Gaussian cumulative distribution function. The mathematical form of the rise-time function is given by the following equation

$$F(t) = \int_{t_{min}}^{t_m} \frac{1}{\sqrt{2\pi}\sigma^2}(X) \left(-\frac{(X-m)^2}{2\sigma^2} \right) dX \quad (6)$$

with $t_{min} = 0$. Values of the rise-time were assumed as follows : $t_m = 10^{-6} \text{ s}$ and $t_m = 10^{-7} \text{ s}$. Values of constants in Eq.(6) are $m = 0.5$ and $\sigma = 0.125$.

In the FE codes available on the market the constitutive relations are usually quite simple and do not specifically tailored to particular problems. All problems of plastic instabilities including thermal coupling must be analyzed with a precise and reliable

In the FE codes available on the market the constitutive relations are usually quite simple and do not specifically tailored to particular problems. All problems of plastic instabilities including thermal coupling must be analyzed with a precise and reliable constitutive relation or relations. A model chosen reflects later the find results. In order to approximate adiabatic instabilities, localization and wave effects, constitutive relations must include strain hardening, rate sensitivity and temperature sensitivity of the flow stress within a wide range of strains, strain rates and temperatures. Again, the constitutive relations, Eqs.(1) to (3), were applied in the numerical analyses of the infinite layer. The final result of those calculations are shown in Fig.50 and Fig.51. In Fig.50 the nominal and the final localization strains are shown as a function of the impact velocity for the rise-time 10^{-6} 1/s. In Fig.51 the total energy to the final localization is shown as a function of the impact velocity. The analogous results for the rise-time 100 ns are shown in Fig.52 and Fig.53.

It may be shown that in the isothermal conditions of deformation, that is at a very low strain rate and the absence of the thermal softening, the instability strain in shear predicted by the constitutive model is infinite. When the impact velocity is increased, beginning from $V_i=0.2$ m/s ($\Gamma_n^Y = 100$ s⁻¹) the instability strain becomes finite. Thus, an increase of the imposed velocity V_i leads to a decrease of the critical strain of localization up to ~ 15 m/s (rise-time 1.0 μ s) and next the critical strain increases due to a positive rate sensitivity, Fig.50. The most substantial change in the instability and localization strains Γ_{nc} occurs between velocities $V_i=120$ m/s and $V_i=170$ m/s, values of Γ_{nc} drop respectively to 0.45 and 0.15. The localization strain drops substantially within this region of strain rates, this is transition to the CIV in shear.

The transition from isothermal to adiabatic regimes of fracturing is more clear when the plastic energy to fracture is analyzed as a function of the logarithm of strain rate, Fig.51 for the rise time 1.0 μ s. Within the domain of lower impact velocities, up to 120 m/s, the energy increases at increasing strain rates. The maximum level is about 600 MJ/m³. At impact velocity 200 m/s the plastic energy to fracture is very low, ~ 100 MJ/m³. Such behavior is caused by superposition of plastic stress waves and a local adiabatic instability, this is again confirmation of the CIV in shear. For the case of rise-time 100 ns the situation is more "chaotic", the transition begins at lower impact velocities, and perturbations are quite high due to wave reflections from the bottom of the layer. At higher strain rates the energies drop again to a very low level, Fig.53. It may be stated that the rise-time 100 ns is too short, even for the case of perforation at, say 2000 m/s, and the results are more correct for longer rise-times.

The energy analyses resemble very closely the ductile-brittle transition observed in fracture mechanics for an isolated crack when the loading rates are increased from quasi-static to impact, but the physical reasons are quite different. This transition is caused by the CIV in shear.

In order to demonstrate the transition to the CIV in shear, Fig.54 shows the spatial distribution of deformation (the shear component) and Fig.55 the temperature distribution in Kelvins for five impact velocities. The figures are referred to the symmetry plane of the specimen and to the final stage of localization. At lower impact velocities, due to the geometry imperfection, the localization occurs in the middle of the layer, that is in the cross-section B (distance 1.0 mm from the support) whereas at impact velocities higher than 100 m/s localization occurs near the layer A (distance 2.0 mm), where the impact occurs, velocities 135 m/s and 170 m/s. The temperature distributions, Fig.55, are similar. At lower impact velocities the

maximums are in the middle of the layer (layer B) reaching value ~ 750 K, but at two highest velocities the maximums are close to the top (layer A) reaching values approaching the melting point.

This transition is demonstrated in different way in Figs.56 and 57 where the evolution of the local shear strains at points A and B as a function of the nominal shear strain are shown for two impact velocities : $V_i = 10$ m/s and $V_i = 150$ m/s. The most important is the COMPLETE change in the evolution of deformation in layers A and B , from the "quasi-static" mode to pure "dynamic" mode. The difference in the shear strain evolution in cross-sections A and B as a function of the nominal strain Γ_n , that is the Marciniak plots, show how the transition occurs from the "quasi-static" strain field to the CIV in shear. Although the nominal strain rate in Fig.

56 is $\dot{\Gamma} = 2 * 10^4 \text{ s}^{-1}$ the evolution of Γ_A and Γ_B is typical for a layer with an imperfection deformed quasi-statically. On the contrary the Marciniak plot shown in Fig.57 for $V = 150$ m/s is completely inverted, the bulk of plastic deformation and localization occurs in the cross-section A, the evolution of plastic deformation in the cross-section B is substantially reduced. It indicates that the impact velocity 150 m/s is already higher than the CIV in shear. At impact velocity $V = 150$ m/s practically all plastic deformation is localized in the layer A indicating on the wave trapping of plastic shearing. The local strain rates in the cross-section A are also very high, for example for $V_i = 130$ m/s, $\dot{\Gamma} \approx 2 * 10^6 \text{ s}^{-1}$. It is interesting to note that at high impact velocities, but lower than the CIV, the maximums of strain rate and temperature are shifted off-center, Figs.54 an 55. This is probably caused by the plastic wave propagation in the layer interior.

The most important observation is that the $\tau_A(\Gamma_n)$ curves differ substantially at different impact velocities. This is demonstrated in Fig 58 for the range of impact velocities from 10 m/s to 200 m/s. In the range of lower impact velocities the $\tau_A(\Gamma_n)$ curves reflect a real behavior of material, this is true up to $V_i \sim 40$ m/s, $\dot{\Gamma} \sim 2 * 10^4 \text{ s}^{-1}$. The $\tau_A(\Gamma_n)$ curve determined at this velocity shows characteristic peak of stress at very small strains. In addition, the initial slope in the "elastic" range becomes much steeper than predicted by the shear modulus. This is caused by interaction of plastic waves and adiabatic instability near the cross-section A. When the impact velocities are still higher, the maximum of shear stress occurs at very small nominal strains, Fig.58.

The slopes $(\partial\tau / \partial\Gamma)_A$ after the stress maximums are negative and they decrease very rapidly when the impact velocities are high enough. This indicates that the CIV is reached. The instability points appear almost instantaneously with more and more shorter process of localization. At low velocities the slopes are equal to μ , but at higher loading rates they are much steeper. The normalized slopes depend also on the rise-time.

The sequence of previous figures clearly demonstrates a substantial evolution of shear stress $\tau_A(\Gamma_n)$ determined at $y = h$, when the impact velocity is increased. Such curves can be determined from the MDS tests. The set of all values of Γ_{nc} and Γ_{nl} determined by the FE analysis shown in Figs.50 and 51 as a function of the impact velocity V_i and the sequence of points indicate for a complicated interplay of thermal coupling and wave processes. Three regions can be recognized, in the first one the ratio of the localization strain Γ_{nl} to the instability strain Γ_{nc} is almost constant. The second region from $V = 120$ m/s is characterized by the beginning of

the thermoplastic deformation trapping by plastic waves. Finally, in the third region at impact velocities higher than 150 m/s the trapping is complete and instantaneous instability and localization occurs with a very small localization strain, typically Γ_{nl} is of the order ~0.08.

It is clear that the phenomenon of the CIV is a PROCESS where the transition is note instantaneous. Consequently, the analytic solutions for the CIV, as presented first time in [3] can not provide an exact value of the CIV but only a crude estimation. Usually such estimation gives the CIV value at the beginning of transition. The evolution of maximum values of shear strain and temperature as a function of the nominal strain $\Gamma_n = \Delta x / h_s$ confirms the physical intuition.

The CIV in shear has a far reaching consequences in fragmentation and perforation. Experiments performed with MDS specimens made of Ti-6Al-4V alloy clearly indicate on a decrease of the fracturing energy when the impact velocity exceeded ~100 m/s. The estimation of energy to failure by the FE method as a function of the impact velocity, in such case the $\tau_A(\Gamma_n)$ curves have been integrated up to the localization strain Γ_{nl} , leads to the conclusion that in the second region a considerable decrease occurs, that is for the impact velocity $V_i = 100$ m/s and higher. In the third region the fracture energy stays almost constant on the level ~100 MJ/m³. Thus, the energy drops practically six times.

8. Discussion and Final Conclusions

This study was to focussed on finding the resistance of Ti-6Al-4V alloy to formation of Adiabatic Shear Bands (ASB) at different impact velocities including the range of velocities up to 100 m/s where the Critical Impact Velocity (CIV) in shear may occur. In order to gather more information on the role of stress concentrators in formation of the ASB's a series of tests with the modified double shear technique (MDS) has been completed with the standard specimen geometry. In order to complete numerical analyses an advanced constitutive relation has been proposed and all material constants for Ti-6Al-4V have been identified.

It was found that the stress concentrators are more and more acute when impact velocity is increased. In addition, a series of FE calculations performed for two cases, that is the standard geometry, Fig.38, and the infinite layer with geometrical imperfection, have shown, as it has been confirmed earlier [16], that large local deformations and locally high strain rates trigger ASB's.

High increments of temperature within the core of the ASB tip reduce, to some extend, a quasi-brittle fracture, if the hardness is sufficiently high, and promotes a local development of the ASB, which can propagate later with a high speed, for example [21].

The stress concentrators increase locally the shear strain rate and temperature reducing at the same time the volume of a material resisting to the imposed load. Although a material may show in a bulk some resistance to fracture and adiabatic shear banding, stress concentrators diminish the VOLUME within which that resistance takes place. Such scenario explains reduction of the failure energy at higher loading rates. This is the case of more brittle alloys with a low ability to strain hardening and relatively high level of hardness. If an alloy exhibits more plasticity the stress concentrators will be "relaxed" by the bulk plastic flow. In such case the failure energy will increase steadily up to the first sign of the CIV and next will drop abruptly, as it is demonstrated in Fig.51.

A clear picture emerges from the scenarios given above. All effects under discussion , that is the ability to strain hardening, rate- and temperature sensitivities, adiabatic increase of temperature, stress concentrators and the CIV in shear, play an important role in resistance to impact loading and fragmentation. The thermal treatment and the final microstructure are the key factors in the optimization process. Combination of plasticity and a high fracture toughness is difficult to achieve.

Acknowledgements

The research reported herein was sponsored in part by the US Army trough its European Research Office, Contract N° : N68171-98-M-5829, and in part by CNRS-France. Acknowledgement are also due to Dr. W.A.Gooch of ARO - USA for fruitful discussions.

REFERENCES

- [1] J.R.Klepaczko, An experimental technique for shear testing at high and very high strain rates. The case of a mild steel, Int. J. Impact Engng., **15** (1994), pp. 25-39.
- [2] J.R.Klepaczko, Experimental Investigation of Adiabatic Shear Banding at Different Impact Velocities, Final Technical Report for the US Army European Res. Office, Contract DAJA 49-90-C-0052, LPMM, Metz University, (1993).
- [3] J.R.Klepaczko, Plastic shearing at high and very high strain rates, Proc. Int. Conf. EURODYMAT 94, J. de Physique IV, Coll. C8, **4** (1994), pp.C8-35 - C8 -40.
- [4] M.Klosak and J.R.Klepaczko, Numerical study of the Critical Impact Velocity in Shear, Appendix N° 1, Final Technical Report prepared for the US Army European Res. Office, Contract DAJA N68171-95-C-9071, LPMM, Metz University (1996).
- [5] Y.Me-Bar and Z.Rosenberg, On the Correlation Between the Ballistic Behavior and Dynamic Properties of Titanium-alloy Plates, Int. J. Impact Engng. , **19** (1997), pp. 311-318.
- [6] L.W.Meyer, L.Krueger, W.A.Gooch and M.S.Burkins, Analysis of Shear Band Effects in Titanium Relative to High Strain-rate Laboratory/Ballistic Impact Tests, Proc. Int. Conf. EURODYMAT 97, J.de Physique IV, (1997), pp.
- [7] I.V.Varfolomeyev and J.R.Klepaczko, Approximate Analysis on Strain Rate Effects and Behavior of Stress and Strain Fields at Crack Tip in Mode II in Metallic Materials, Appendix N° 1 to the Technical Report for the US Army European Res. Office, Contract DAJA 49-90-C-0052, LPMM, Metz University (1992).
- [8] J.R.Klepaczko and B.Rezaig, A numerical study of adiabatic shear banding in mild steel by dislocation mechanics based constitutive relations , Mechanics of Materials, **24** (1996), pp.125-139.
- [9] J.R.Klepaczko, Stress Concentrators and Rate Effects in Formation of Adiabatic Shear Bands, Technical Report for the US Army European Res. Office, Contract N68171-95-C-9071, LPMM, Metz University (1996).
- [10] J.R.Klepaczko and M. Klosak, Numerical study of the critical impact velocity in shear, Eur. J. Mech., A/Solids, **18** (1999), pp. 93-113.
- [11] T.Kàrmàn and P.E.Duvez, The propagation of plastic deformation in solids, J. Appl. Phys., **21** (1950), pp. 987-994.

- [12] J.W.Swiegle and D.B.Grady, Calculation of thermal trapping in shear bands, in:
Metallurgical Application of Shock-Wave and High-Strain Rate Phenomena,
Marcel Dekker, Inc., N.Y. (1986), pp. 705-722.
- [13] J.R.Klepaczko, Generalized conditions for stability in tension test, Int. J. Mech.
Sci., **10** (1968), pp.297-313.
- [14] D.C.Erlach, D.R.Curran and L.Seaman, Further Development of a
Computational Shear Band Model, Report AMMRC TR80-3, SRI International
(1980).
- [15] Martin G.H.Wells, The Mechanical and Ballistic Properties of an Electron
Beam Single Melt of Ti-6Al-4V Plate, AMSRL-WM-MC, (Spt. 1998).
- [16] J.R.Klepaczko, Stress Concentrators and Rate Effects in Formation of
Adiabatic Shear Bands, Technical Report for the European Res. Office of the
US Army, Contract N°: N68171-97-C-9003, (1998).
- [17] J.R.Klepaczko, Recent progress in testing of materials in impact shearing ,
Proc.of the 1995 Joint ASME/JSME Pressure Vessels and Piping Conf. PVP
-Vol.300, Dynamic Fracture, Failure, and Deformation, ASME (1995),
pp. 165-173.
- [18] J.R.Klepaczko, A practical stress-strain strain-rate temperature constitutive
relation of the power form, J. Mech. Working Technology, **15** (1987),
pp.143-165.
- [19] ABAQUS Manual, Version 5.5, Hibbit, Karlsson and Sorensen, Inc.,
Providence, RI, USA (1995).
- [20] A.S.Lebouvier and J.R.Klepaczko, Numerical study of fast shearing and the
critical impact velocity in shear, case of Ti-6Al-4V, Paper in preparation.
- [21] M. Zhou, A. J. Rosakis and G. Ravichandran, Dynamically Propagating Shear
Bands in Impact-Loaded Prenotched Plates, SM Report 94-01, California Inst. of
Technology, Pasadena, CA (1995).

TABLES

- TAB. 1 Listing of quasi-static tests.
- TAB. 2 Listing of direct impact tests.
- TAB. 3 Material constants in the constitutive relations.
- TAB. 4 Material constants in thermal coupling.

FIGURE CAPTIONS

- Fig. 1 Proof Stress and Tensile Strength as a function of temperature for Ti-6Al-4V , grade 5.
- Fig. 2 Elongation over gage length 50 mm as a function of temperature for Ti-6Al-4V, grade 5.
- Fig. 3 Modified Double Shear (MDS) specimen, standard geometry.
- Fig. 4 Device for quasi-static loading of the MDS specimen; 1-base plate, 2- specimen support, 3- MDS specimen, 4- punch, 5- LVDT displacement gage, 6- load cell.
- Fig. 5 Configuration of experimental setup for impact shearing of the MDS Specimen.
- Fig. 6 Oscillogram of a test on MDS specimen with device of Fig.4, (standard geometry).
- Fig. 7 Results of quasi-static tests on MDS specimens, mean curves after three tests, Ti-6Al-4V.
- Fig. 8 Strain rate histories for quasi-static tests, mean curves.
- Fig. 9 Oscillogram of direct impact test, effective impact velocity $V = 3.2 \text{ m/s}$.
- Fig. 10 Oscillogram of direct impact test, effective impact velocity $V = 16.3 \text{ m/s}$.
- Fig. 11 Oscillogram of direct impact test, effective impact velocity $V = 76 \text{ m/s}$.

Fig. 12 Oscillogram of direct impact test, effective impact velocity $V = 98$ m/s.

Fig. 13 Shear stress vs. shear strain curves for two tests, shear strain rate $1.6 \cdot 10^3$ 1/s.

Fig. 14 Shear stress vs. shear strain curves for three tests, shear strain rate $8.1 \cdot 10^3$ 1/s.

Fig. 15 Shear stress vs. shear strain curves for five tests, shear strain rate $4.9 \cdot 10^4$ 1/s.

Fig. 16 Shear stress vs. shear strain curves for four tests, shear strain rate $5.4 \cdot 10^4$ 1/s.

Fig. 17 Strain rate spectrum for the standard geometry for three levels of shear strain, quasi-static range, Ti-6Al-4V.

Fig. 18 Strain rate spectrum for the standard geometry for two levels of shear strain, direct impact method, Ti-6Al-4V.

Fig. 19 Strain rate spectrum for standard geometry at the level of "Proof Stress" with mean points (black circles), Ti-6Al-4V.

Fig. 20 Complete strain rate spectrum at the level of "Proof Stress", Ti-6Al-4V.

Fig. 21 Nominal strain at instability point, $\Gamma_{nc} = \Delta X / h_s$ vs. logarithm of the nominal strain rate V_i / h_s , quasi-static spectrum of strain rate, Ti-6Al-4V.

Fig. 22 Nominal strain at instability point vs. logarithm of the nominal strain rate, direct impact spectrum of strain rate, Ti-6Al-4V.

Fig. 23 Nominal strain at instability point vs. logarithm of the nominal strain rate, complete spectrum for Ti-6Al-4V.

Fig. 24 Theoretical values of the nominal strain at the instability point for the complete spectrum of strain rate, coefficient $a \approx 3.0$.

Fig. 25 SEM picture of fracture surface for the case of quasi-static loading.

Fig. 26 SEM picture of fracture surface for the case of quasi-static loading.

Fig. 27 SEM picture of fracture surface for the case of quasi-static loading.

Fig. 28 SEM picture of fracture surface for the case of quasi-static loading.

Fig. 29 SEM picture of fracture surface for the case of direct impact loading.

Fig. 30 SEM picture of fracture surface for the case of direct impact loading.

Fig. 31 SEM picture of fracture surface for the case of direct impact loading.

Fig. 32 SEM picture of fracture surface for the case of direct impact loading.

Fig. 33 SEM picture of fracture surface for the case of direct impact loading.

Fig. 34 SEM picture of fracture surface for the case of direct impact loading.

Fig. 35 Constitutive surface for yield stress as a function of shear strain and log. of strain rate - upper figure; and as a function of temperature and strain - lower figure, Ti-6Al-4V.

Fig. 36 Theoretical adiabatic and isothermal $\tau(\Gamma)$ curves for strain rate

$$3.8 \times 10^4 \text{ 1/s}$$

Fig. 37 Theoretical adiabatic and isothermal $\tau(\Gamma)$ curves for strain rate $4.9 \times 10^4 \text{ 1/s}$.

Fig. 38 FE mesh applied to simulate MDS specimen, lower part is supported by elastic support (Hopkinson tube), plane strain -2D model, characteristic layers are A, B and C.

Fig. 39 Nominal shear strains of instability Γ_1 ($\alpha = 1.0$) and localization Γ_l ($\alpha = 50$) as a function of normalized strain rate.

Fig. 40 Shear stress τ_c at cross section C vs. nominal shear strain Γ_n determined by FE from displacement of cross-section A for different values of α , impact velocity 100 m/s is close to the CIV.

Fig. 41 Shear stress τ_c at cross section C vs. time determined By FE from displacement of cross section A for $\alpha = 50$, circles denote start and complete failure of the cross section.

Fig. 42 Spatial distributions of shear strain in MDS geometry for imposed velocity 20 m/s at $t = 7.5 \mu\text{s}$, deformation begins in all four stress concentrators.

Fig. 43 Spatial distribution of shear strain in MDS geometry for imposed velocity 20 m/s at $t = 15 \mu\text{s}$, deformation field is more uniform.

Fig. 44 Spatial distribution of shear strain in MDS geometry for imposed velocity 20 m/s at $t = 22.5 \mu\text{s}$, uniform deformation field.

Fig. 45 Spatial distribution of shear strain in MDS geometry for imposed velocity 20 m/s at $t = 30 \mu\text{s}$, ASB is in advanced state.

Fig. 46 Spatial distribution of shear strain in MDS geometry for imposed velocity 100 m/s at $t = 2.0 \mu\text{s}$, ASB starts to propagate at layer A.

Fig. 47 Spatial distribution of shear strain in MDS geometry for imposed velocity 100 m/s at $t = 2.5 \mu\text{s}$, ASB reaches middle of the layer A.

Fig. 48 Spatial distribution of shear strain in MDS geometry for imposed velocity 100 m/s at $t = 3.0 \mu\text{s}$, ASB advances to 3/4 of the layer A.

Fig. 49 Spatial distribution of shear strain in MDS geometry for imposed velocity 100 m/s at $t = 3.5 \mu\text{s}$, close to complete failure by formation of ASB.

Fig. 50 Nominal strain for the instability point and final localization strain for MDS geometry as a function of impact velocity, FE analysis for $a = 50$ and rise-time $1.0 \mu\text{s}$.

Fig. 51 Fracture energy vs. impact velocity V_i , FE analysis for $a = 50$ and rise-time $1.0 \mu\text{s}$.

Fig. 52 Nominal strain for the instability point and final localization strain for MDS geometry as a function of impact velocity, FE analysis for $a = 50$ and rise-time 100 ns .

Fig. 53 Fracture energy vs. impact velocity V_i , FE analysis for $a = 50$ and rise-time 100 ns .

Fig. 54 Evolution of shear strains in the MDS geometry along the height for five impact velocities, FE analysis, distance 0 denotes layer C (support), distance 2 mm denotes layer A (impact side). Above CIV localization occurs at A.

Fig. 55 Evolution of temperatures in the MDS geometry along the height for five Impact velocities, FE analysis, distance 0 denotes layer C (support), distance 2 mm denotes layer A (impact side). Above CIV localization occurs at A.

Fig. 56 Marciniak plot showing evolution of shear-strain in layers A and B at $V_i = 10 \text{ m/s}$, nominal strain rate $5 \times 10^3 \text{ 1/s}$. Strain localization in B.

Fig. 57 Marciniak plot showing evolution of shear-strain in layers A and B at $V_i = 150 \text{ m/s}$, nominal strain rate $7.5 \times 10^4 \text{ 1/s}$. Strain localization in A.

Fig. 58 Reconstituted adiabatic shear stress τ_A of layer A vs. nominal shear-strain Γ_n for seven impact velocities.

Ti-6Al-4V

Files	Strain rate	Critical strain
Ti01v3	1e-2 1/s	0.13000
Ti02v3	1e-2 1/s	0.15000
Ti03v3	1e-2 1/s	0.15500
Ti04v4	9e-2 1/s	0.10000
Ti05v4	9e-2 1/s	0.085000
Ti06v4	9e-2 1/s	0.10000
Ti07v4	9e-2 1/s	0.095000
Ti08v2	1e-3 1/s	
Ti09v2	1e-3 1/s	0.085000
Ti10v2	1e-3 1/s	0.15000
Ti11v2	1e-3 1/s	0.14000
Ti12v5	1 1/s	0.080000
Ti13v5	1 1/s	0.080000
Ti14v5	1 1/s	0.079000
Ti15v5	1 1/s	0.075000
Ti16v6	5 1/s	0.075000
Ti17v6	5 1/s	0.075000
Ti18v6	5 1/s	0.080000
Ti20v7	10 1/s	0.070000
Ti21v7	10 1/s	0.075000
Ti22v7	10 1/s	0.080000

TABLE 1

Ti-6Al-4V

Files	Strain rate	Critical strain
Th01v1	7e3 1/s	0.063456
Th02v1	7e3 1/s	0.089920
Th03v1	7e3 1/s	0.036000
Th04v1	7e3 1/s	0.024933
Th05v2	8,13e3 1/s	0.052536
Th06v2	8,13e3 1/s	0.046895
Th07v2	8,13e3 1/s	0.13293
Th08v2	8,13e3 1/s	0.18269
Th09v3	1,3e4 1/s	0.035970
Th10v3	1,3e4 1/s	0.13420
Th11v3	1,3e4 1/s	0.19221
Th12v0	1,6e3 1/s	0.030504
Th13v0	1,6e3 1/s	0.076398
Th14v0	1,6e3 1/s	0.095179
Th15v4	3,8e4 1/s	0.059749
Th16v4	3,8e4 1/s	0.085970
Th17v4	3,8e4 1/s	0.10471
Th18v5	4,9e4 1/s	0.10039
Th19v5	4,9e4 1/s	0.14188
Th20v5	4,9e4 1/s	
Th21v5	4,9e4 1/s	0.13680
Th22v5	4,9e4 1/s	0.10293
Th23v5	4,9e4 1/s	
Th24v4	3,8e4 1/s	
Th25v4	3,8e4 1/s	
Th26v4	3,8e4 1/s	
Th27v6	5,37e4 1/s	
Th28v6	5,37e4 1/s	
Th29v6	5,37e4 1/s	
Th30v6	5,37e4 1/s	0.024380
Th31v6	5,37e4 1/s	0.077202
Th32v6	5,37e4 1/s	0.068069

TABLE 2

Ti-Al6-V4

$$\tau = \frac{\mu(T)}{\mu_0} \left[B \left(\frac{T}{T_0} \right)^{-v} (\Gamma_0 + \Gamma_p)^n + \tau_0 \left(1 - \frac{T}{D} \log \left(\frac{\dot{\Gamma}_0}{\dot{\Gamma}} \right) \right)^m \right]$$

$$\mu(T) = \mu_0 \left(1 - A T^* - c T^{*2} \right); T^* = T - 300$$

$$n = n_0 \left(1 - \frac{T}{T_f} \right)$$

paramètres	valeurs	unités
B	1053.8	MPa
v	0.113	-
Γ_0	1.6×10^{-3}	-
τ_0	750	MPa
D	4347	K
$\dot{\Gamma}_0$	10^{-6}	s ⁻¹
m	3.4368	-
μ_0	43.91	GPa
A	6.808×10^{-4}	K ⁻¹
C	1.036×10^{-7}	K ⁻²
n_0	0.0336	-
T_f	1900	K

TABLE 3

Ti-6Al-4V

paramètres	valeurs	unités
β	0.9	-
λ		-
ρ	4510	$\text{kg} \cdot \text{m}^{-3}$
C_v	543	$\text{J} \cdot \text{kg}^{-1} \text{K}^{-1}$
T_m	1900	K

TABLE 4

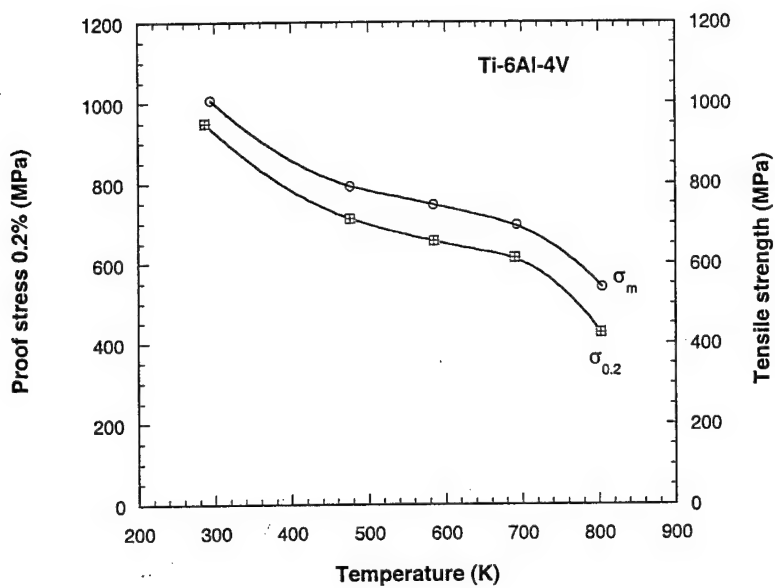


Fig. 1

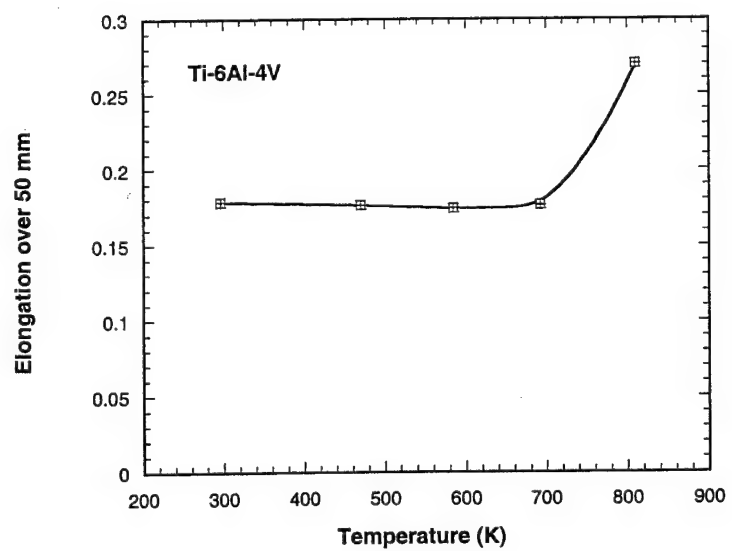


Fig. 2

Eprouvettes de double cisaillement
type 1

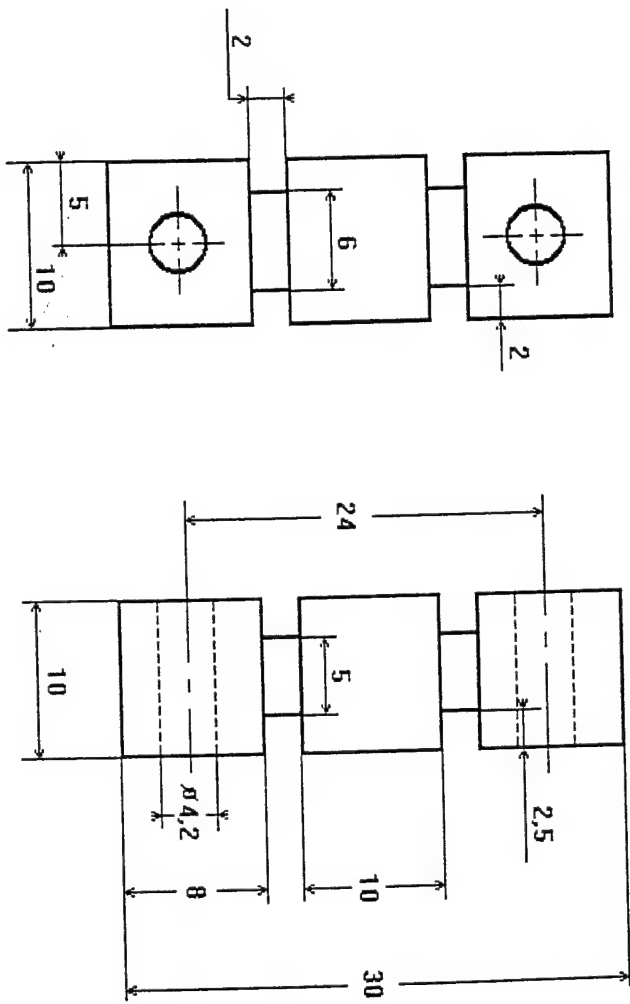


Fig. 3

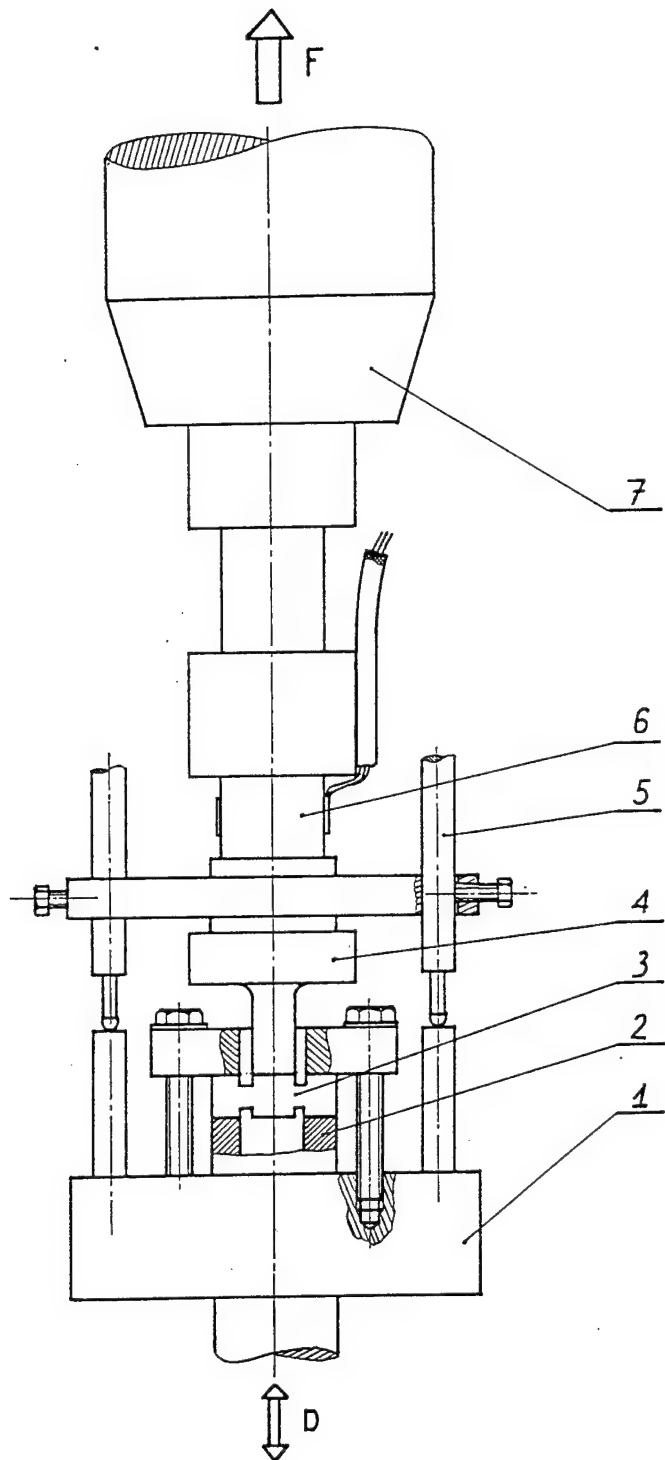


Fig. 4

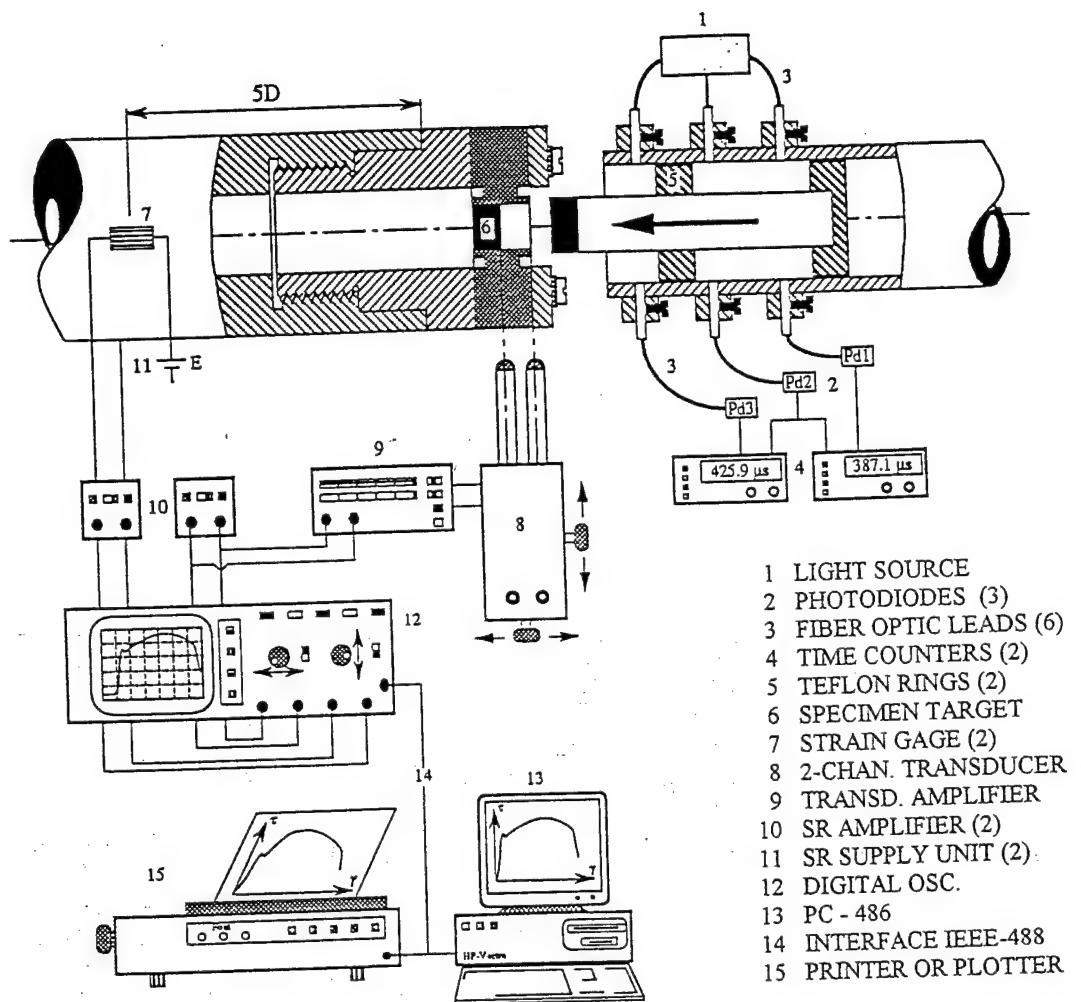


Fig. 5

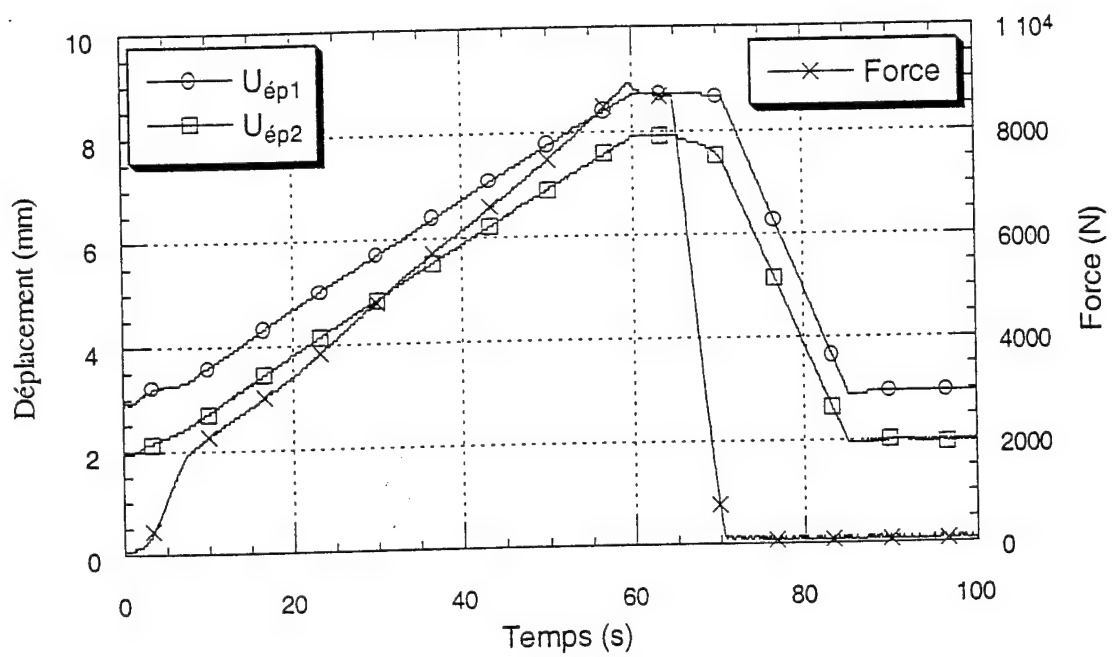


Fig. 6

Ti-6Al-4V

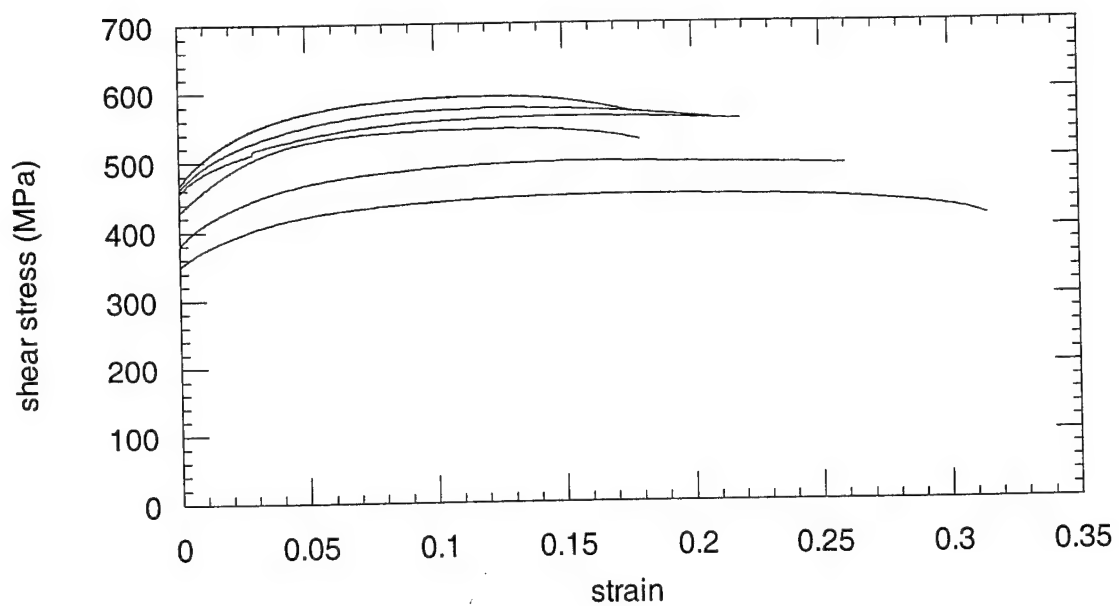


Fig. 7

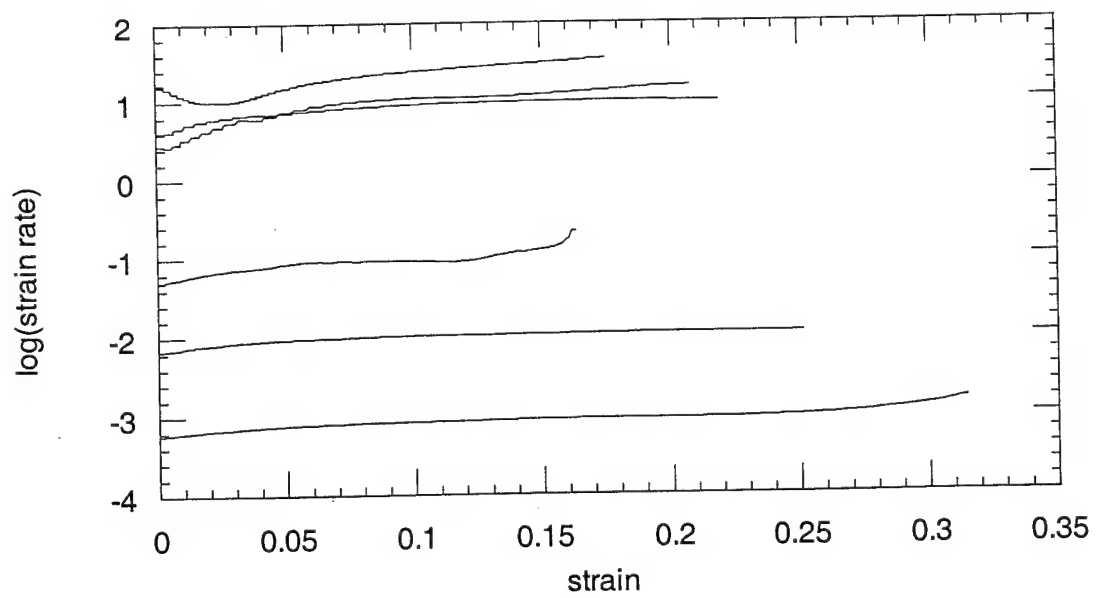


Fig. 8

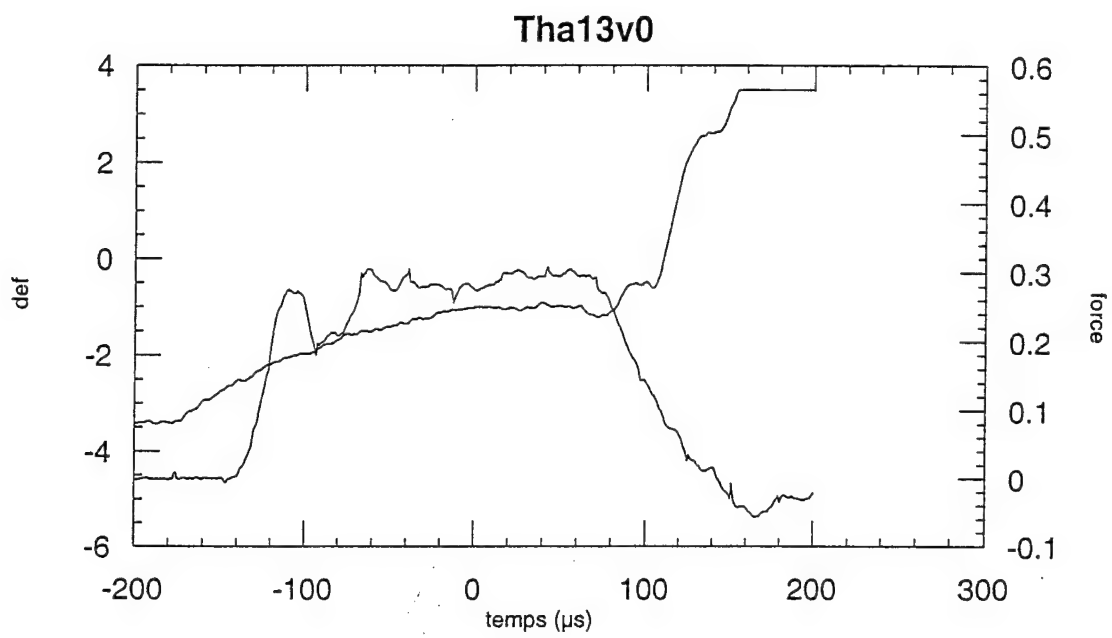


Fig. 9

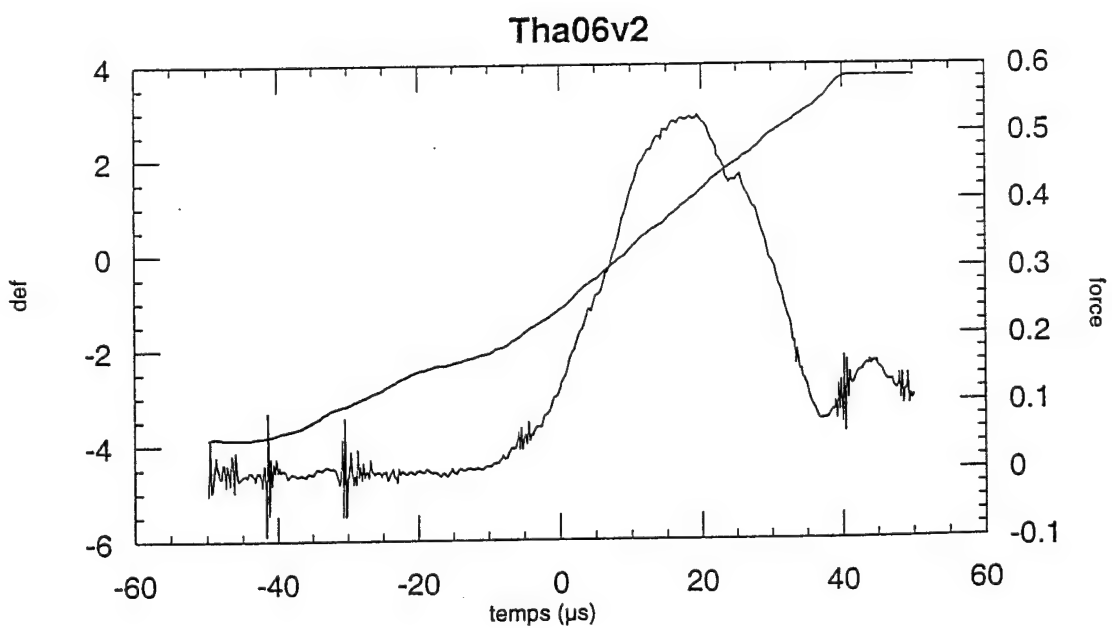


Fig. 10

Tha16v4

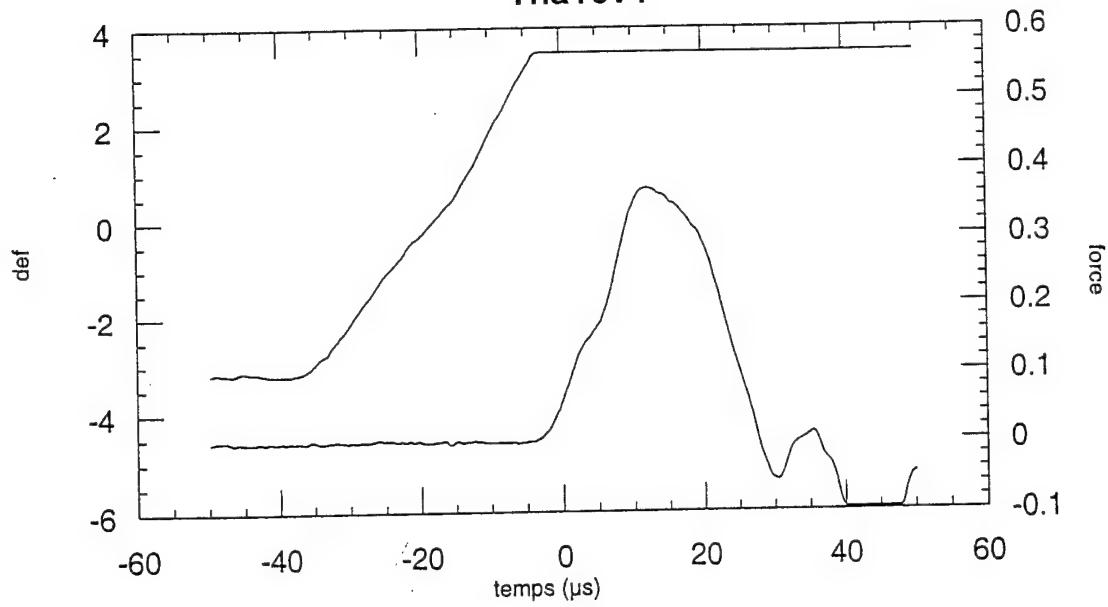


Fig. 11

Tha18v5

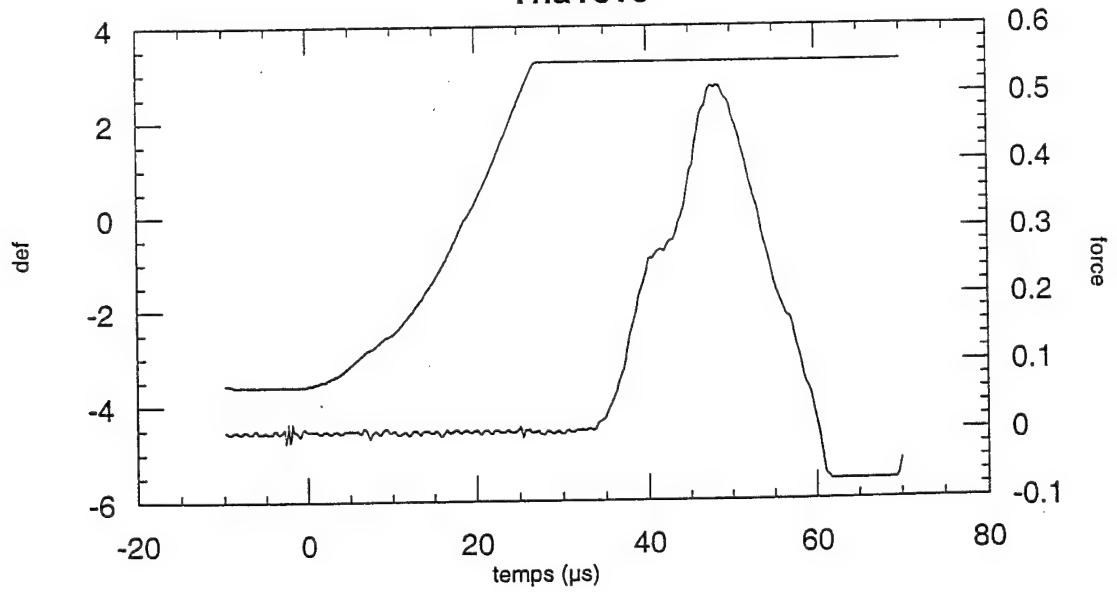


Fig. 12

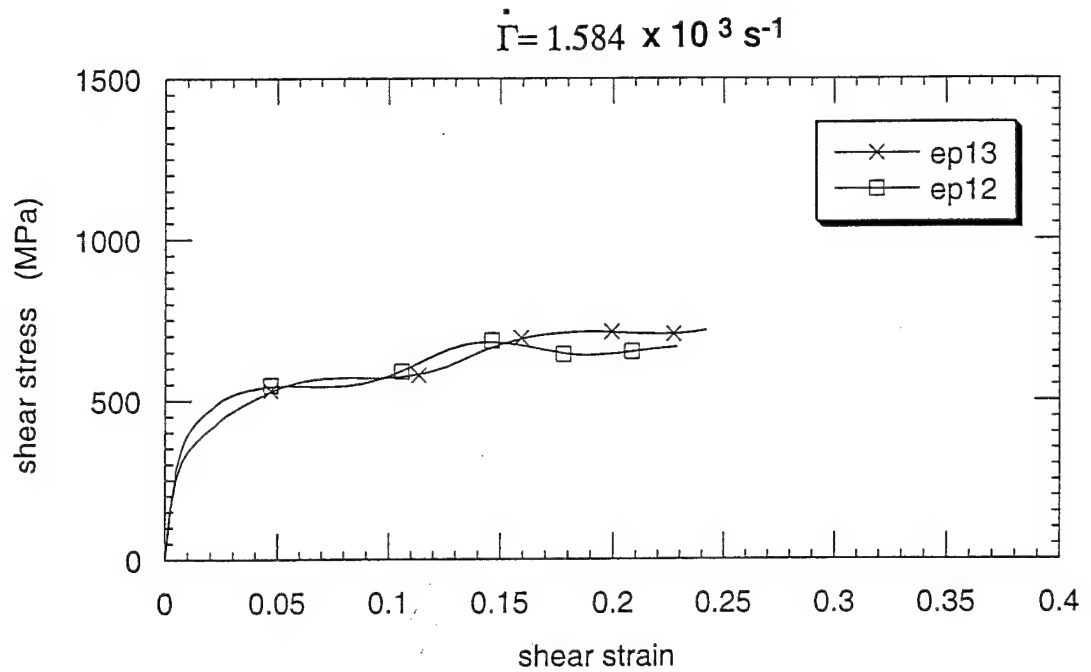


Fig. 13

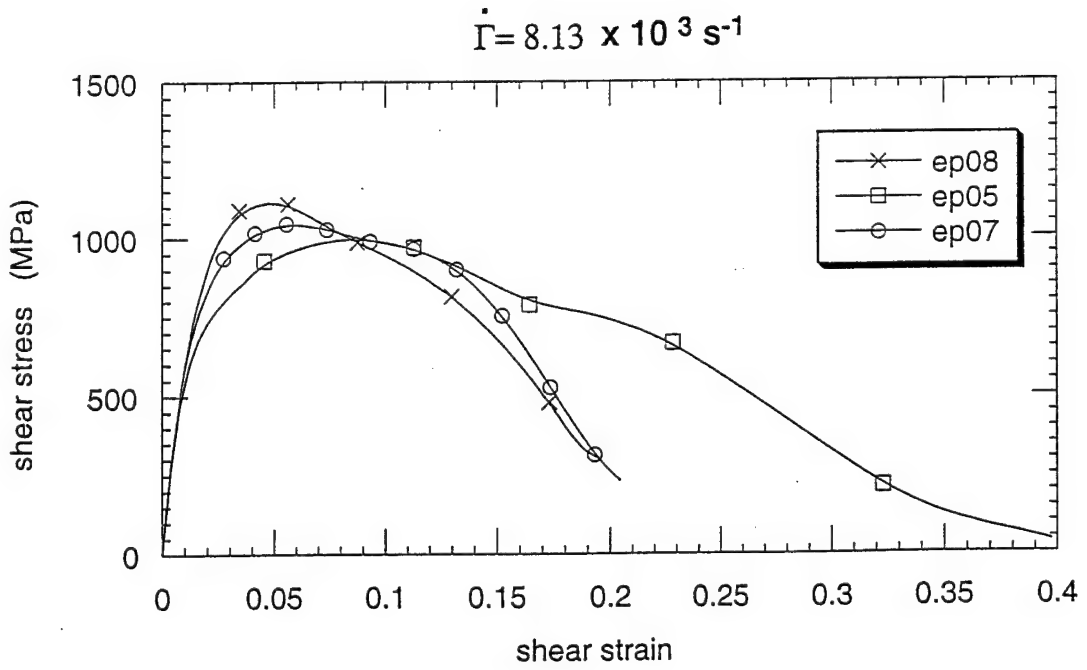


Fig. 14

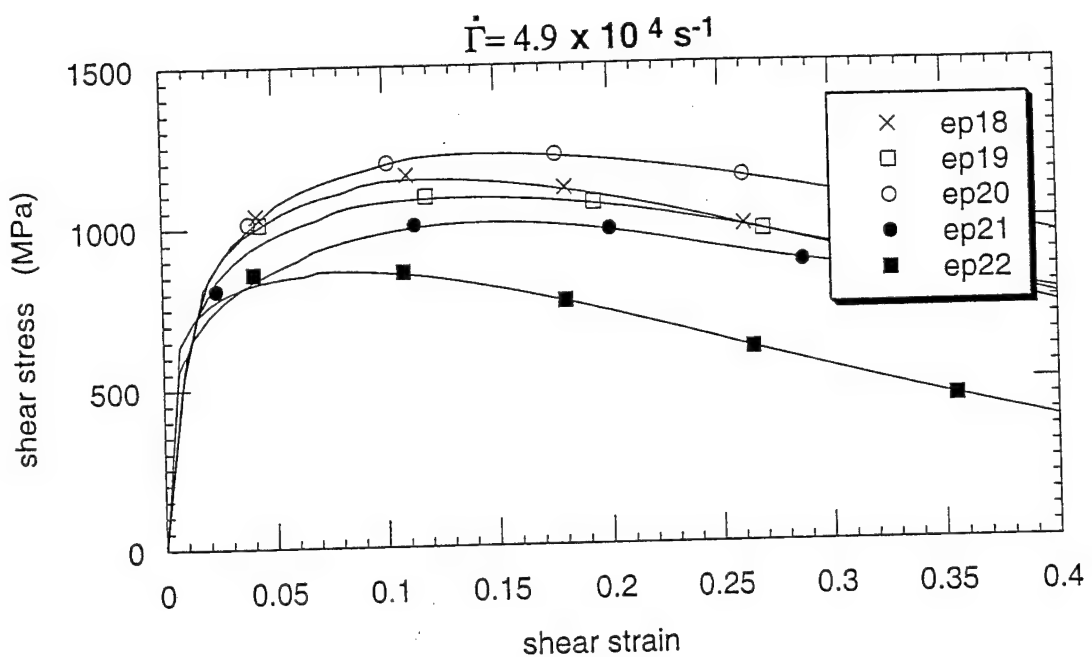


Fig. 15

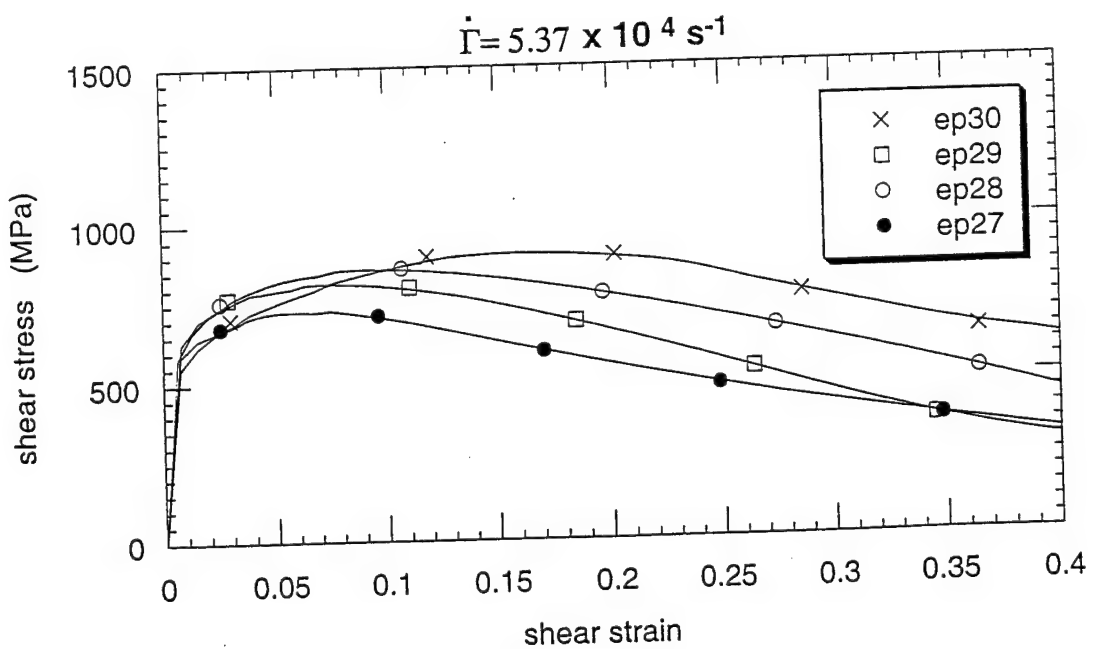


Fig. 16

Ti-6Al-4V

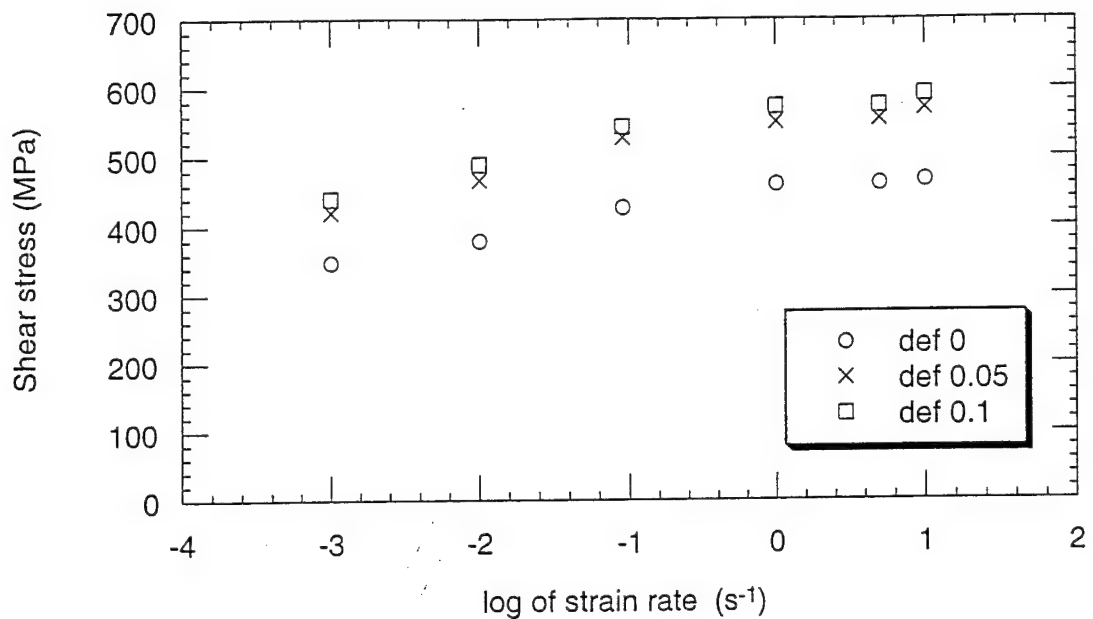


Fig. 17

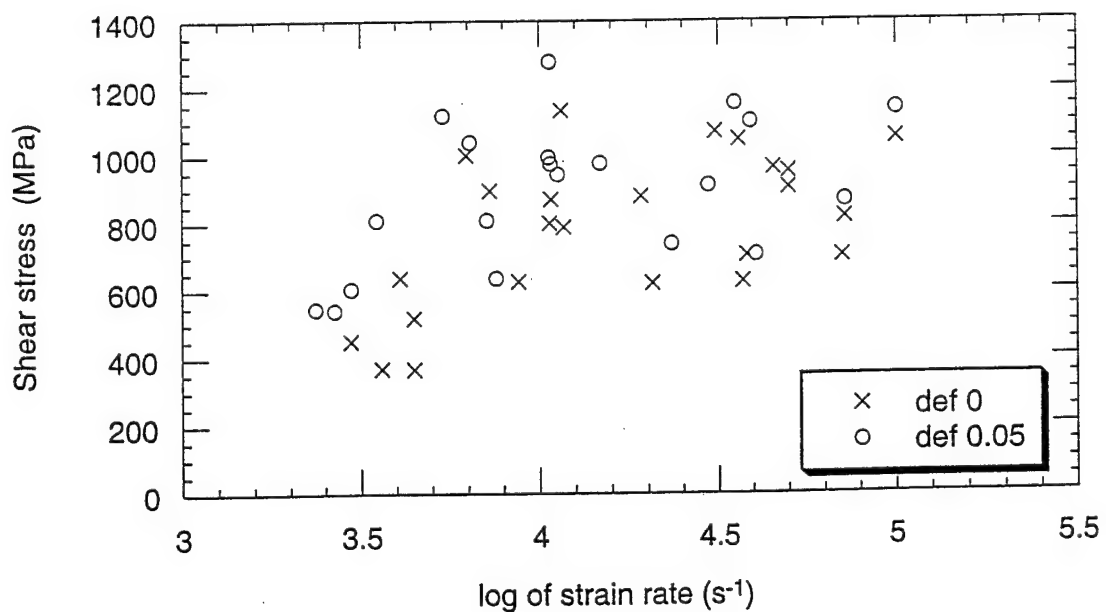


Fig. 18

Ti-6Al-4V

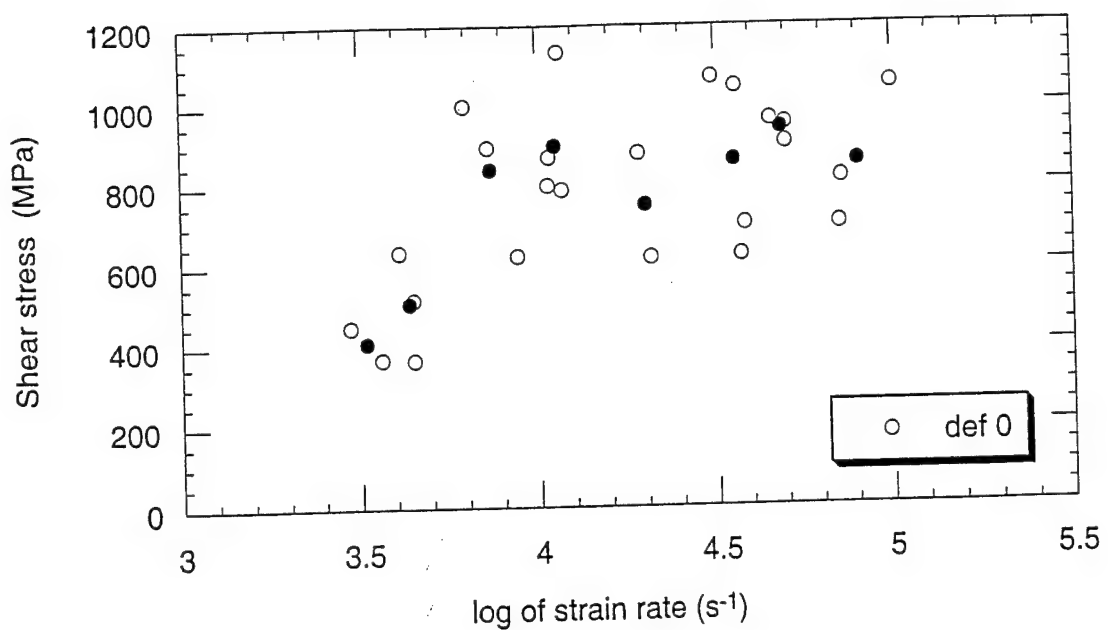


Fig. 19

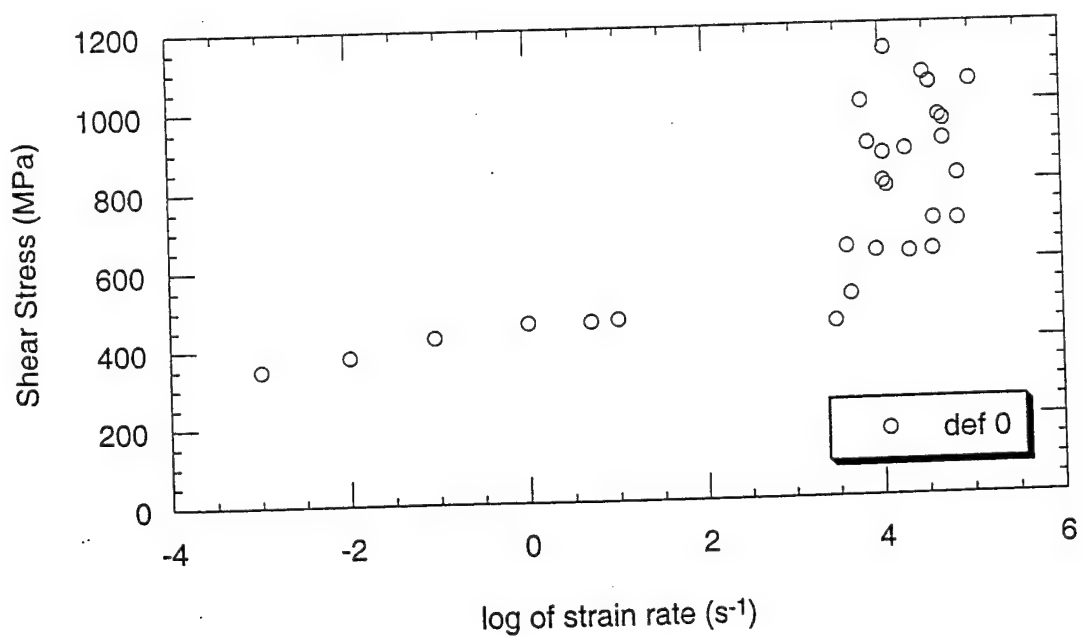


Fig. 20

Ti-6Al-4V

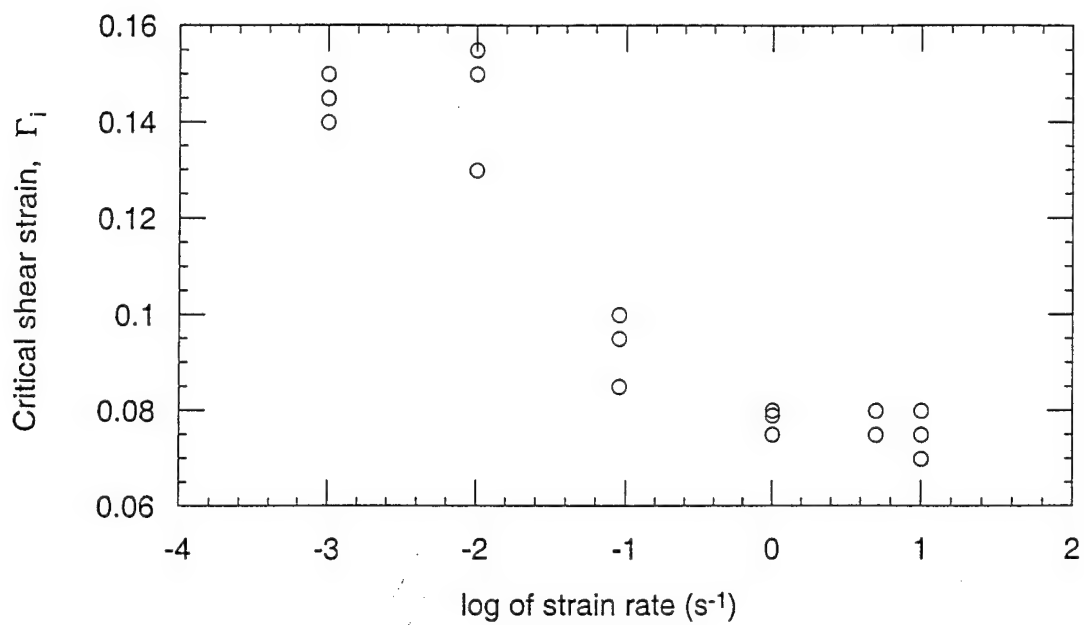


Fig. 21

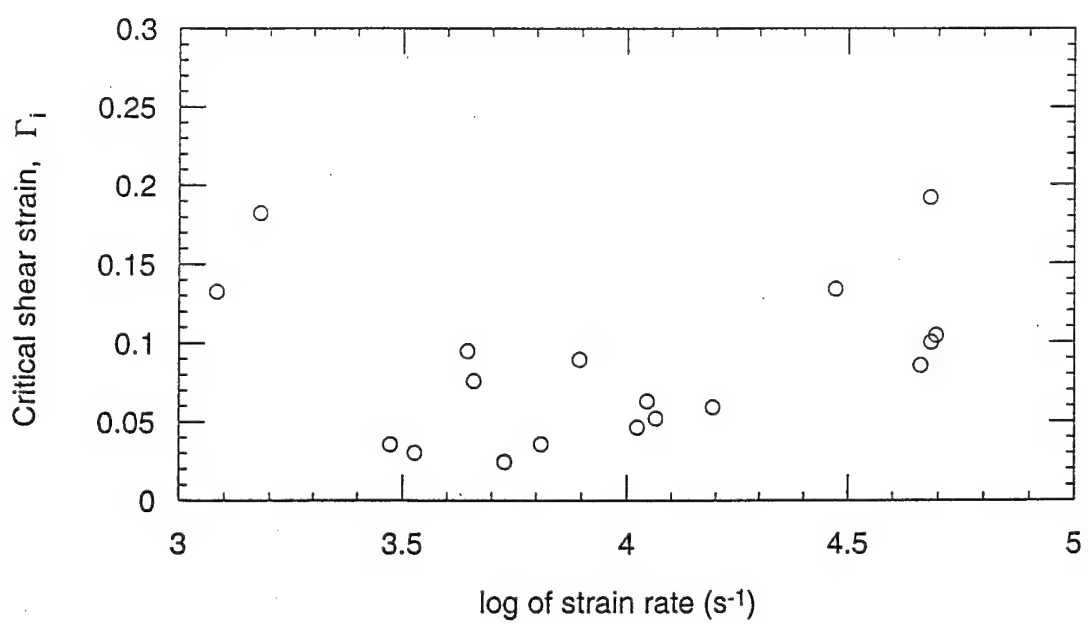


Fig. 22

Ti-6Al-4V

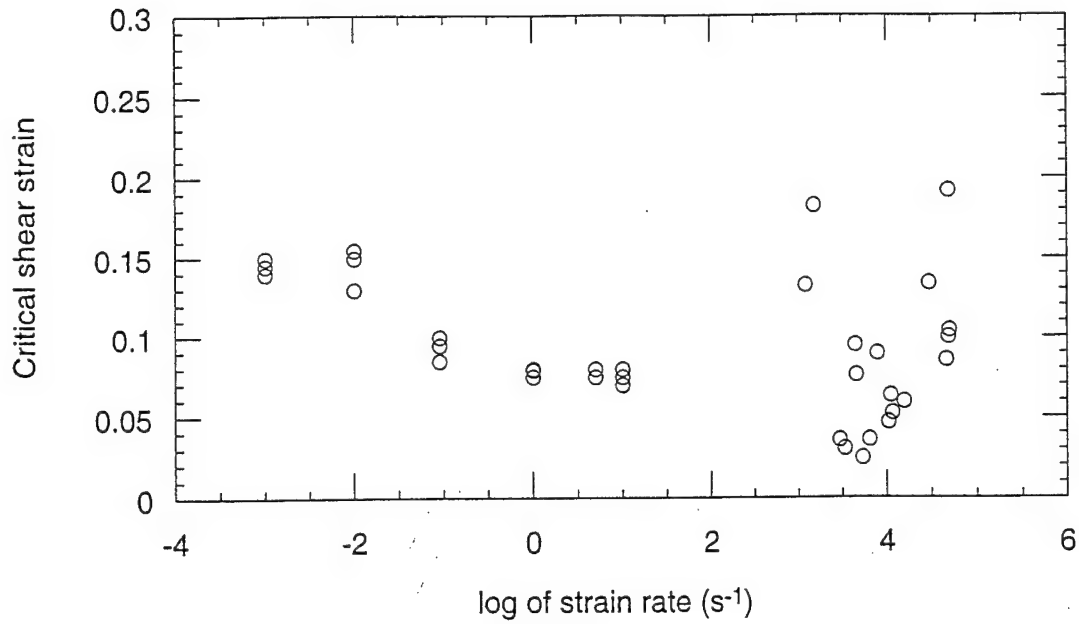


Fig. 23

Ti-6Al-4V

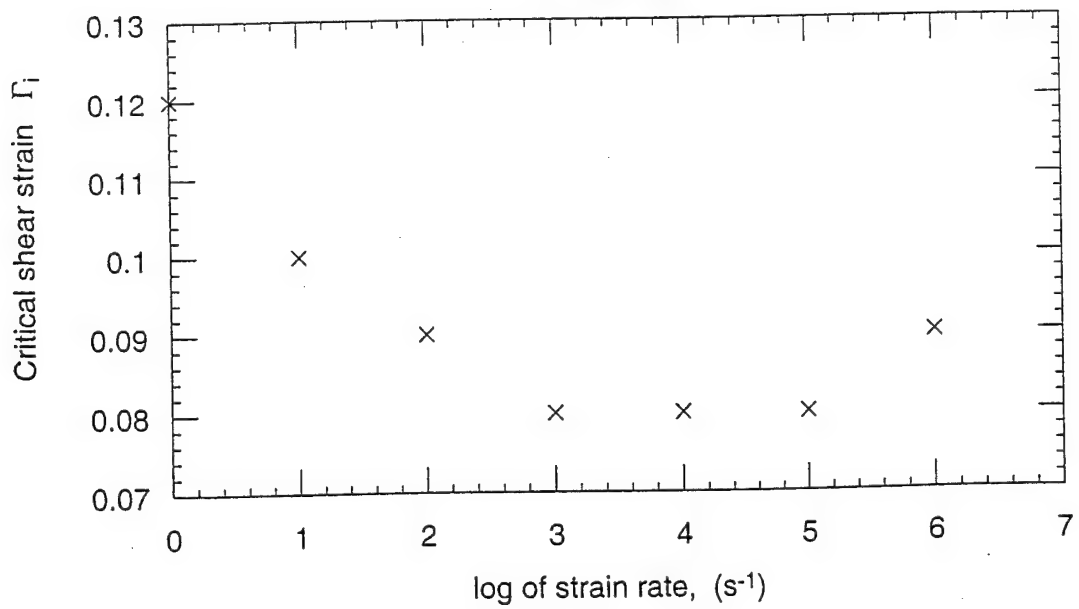


Fig. 24

Ti-6Al-4V Spec. TI09V2 $V_0 = 2^E - 6$ m/s

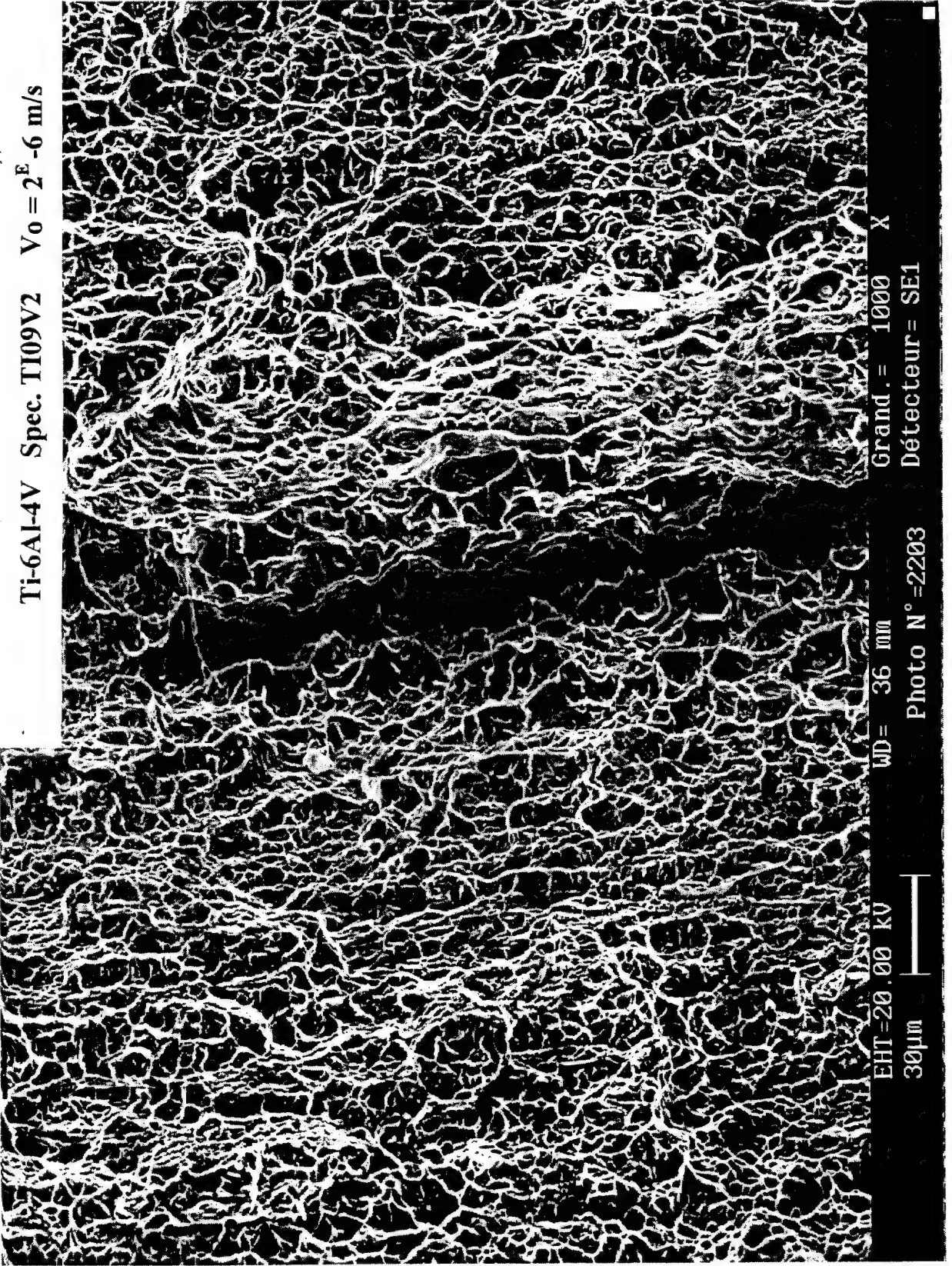


Fig. 25

Ti-6Al-4V Spec. TI09V2 $V_0 = 2^E - 6$ m/s

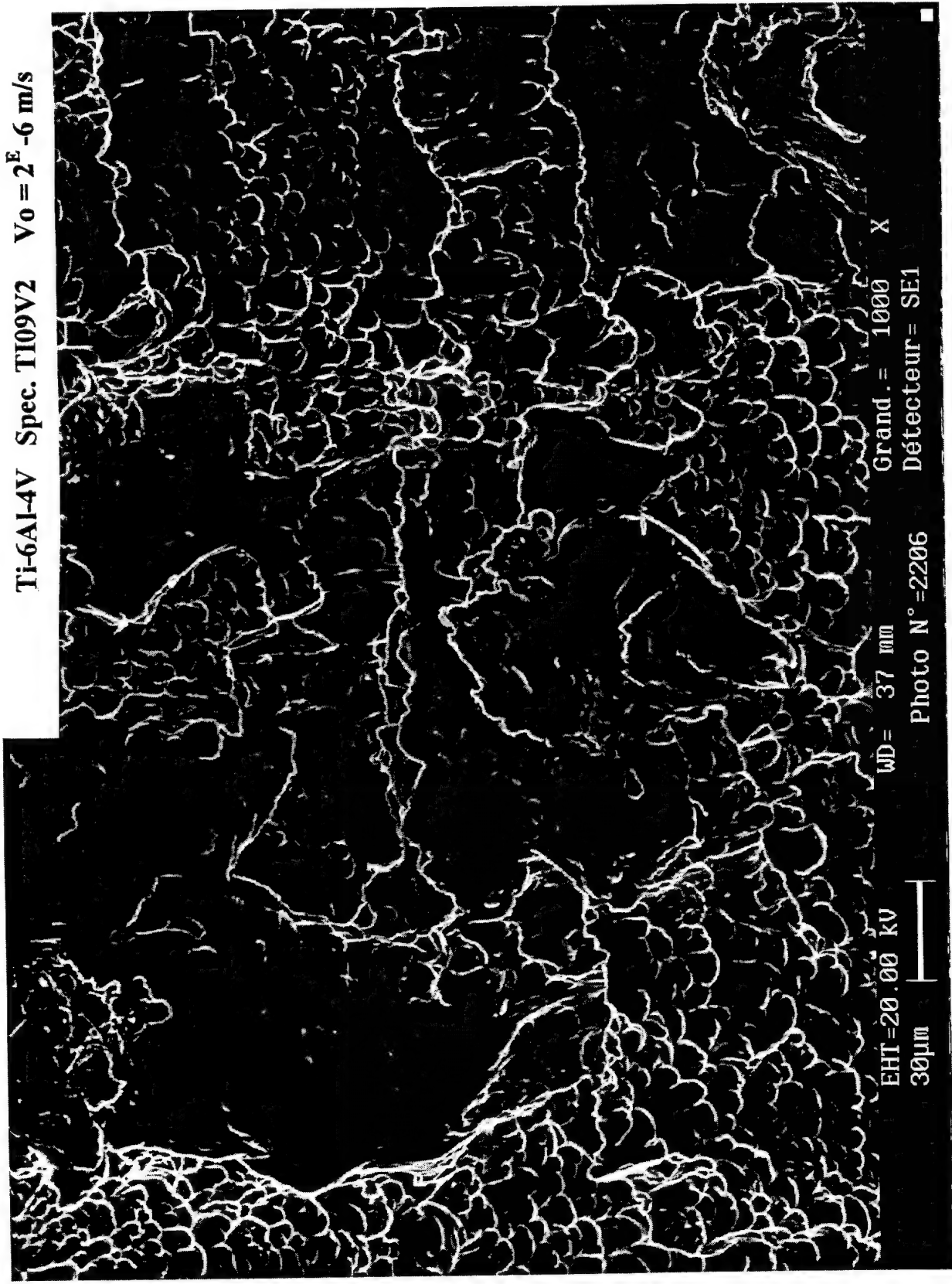


Fig. 26

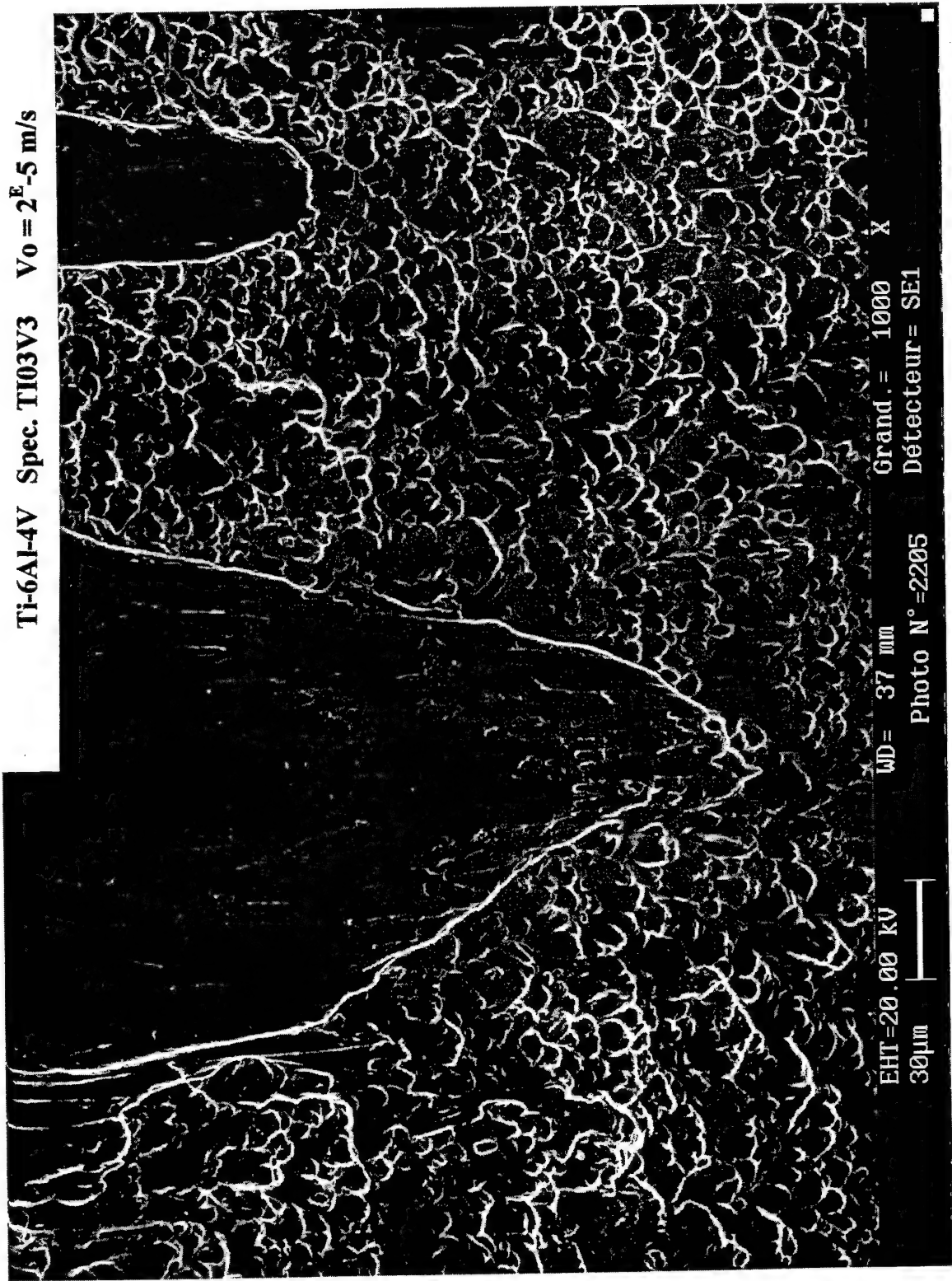


Fig. 27

Ti-6Al-4V Spec. TI03V3 $V_0 = 2^E - 5$ m/s

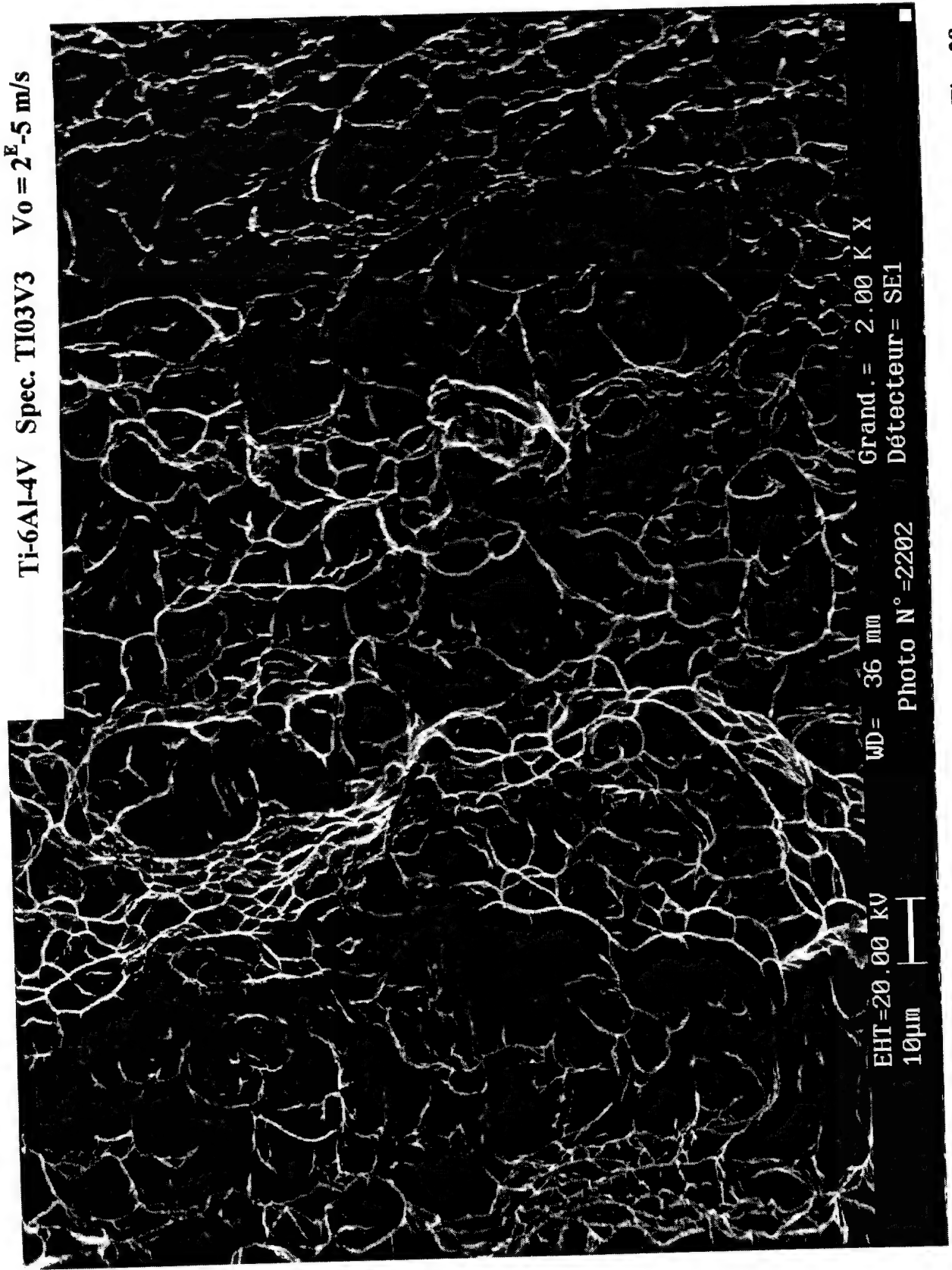


Fig. 28

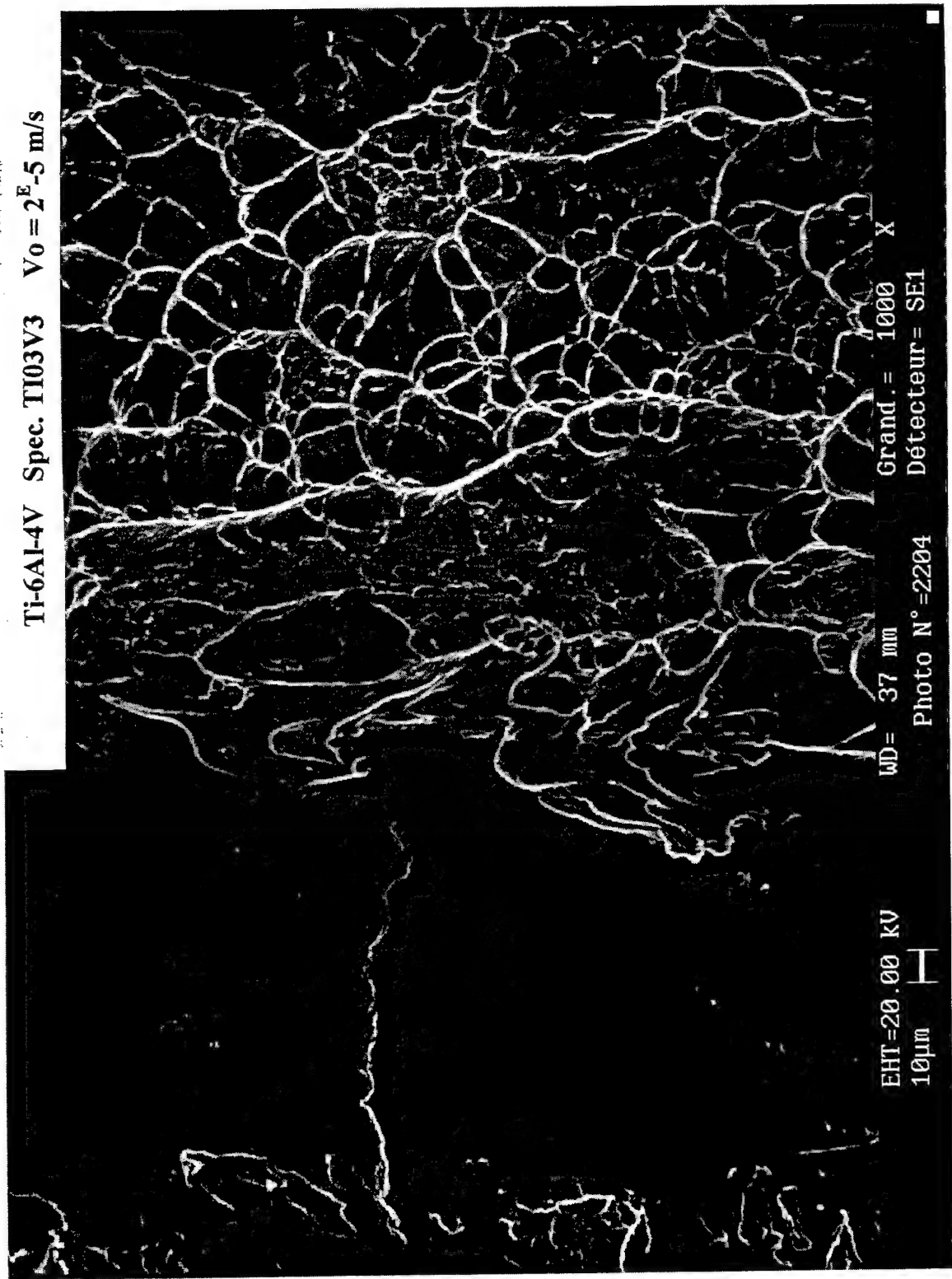


Fig. 29

Ti-6Al-4V Spec. TH18V5 $V_0 = 98.0 \text{ m/s}$

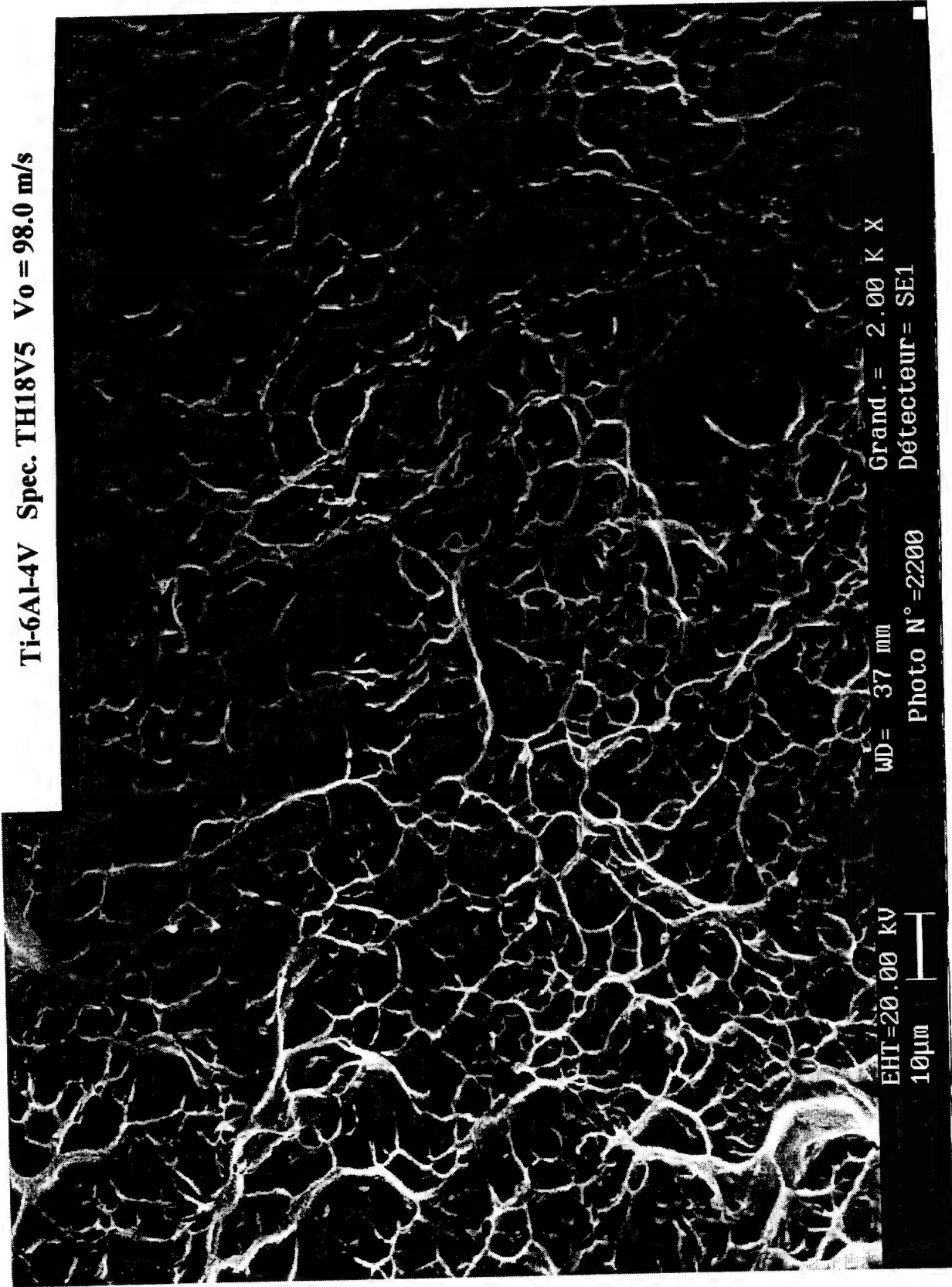


Fig. 30

Ti-6Al-4V Spec. TH18V5 $V_0 = 98.0 \text{ m/s}$

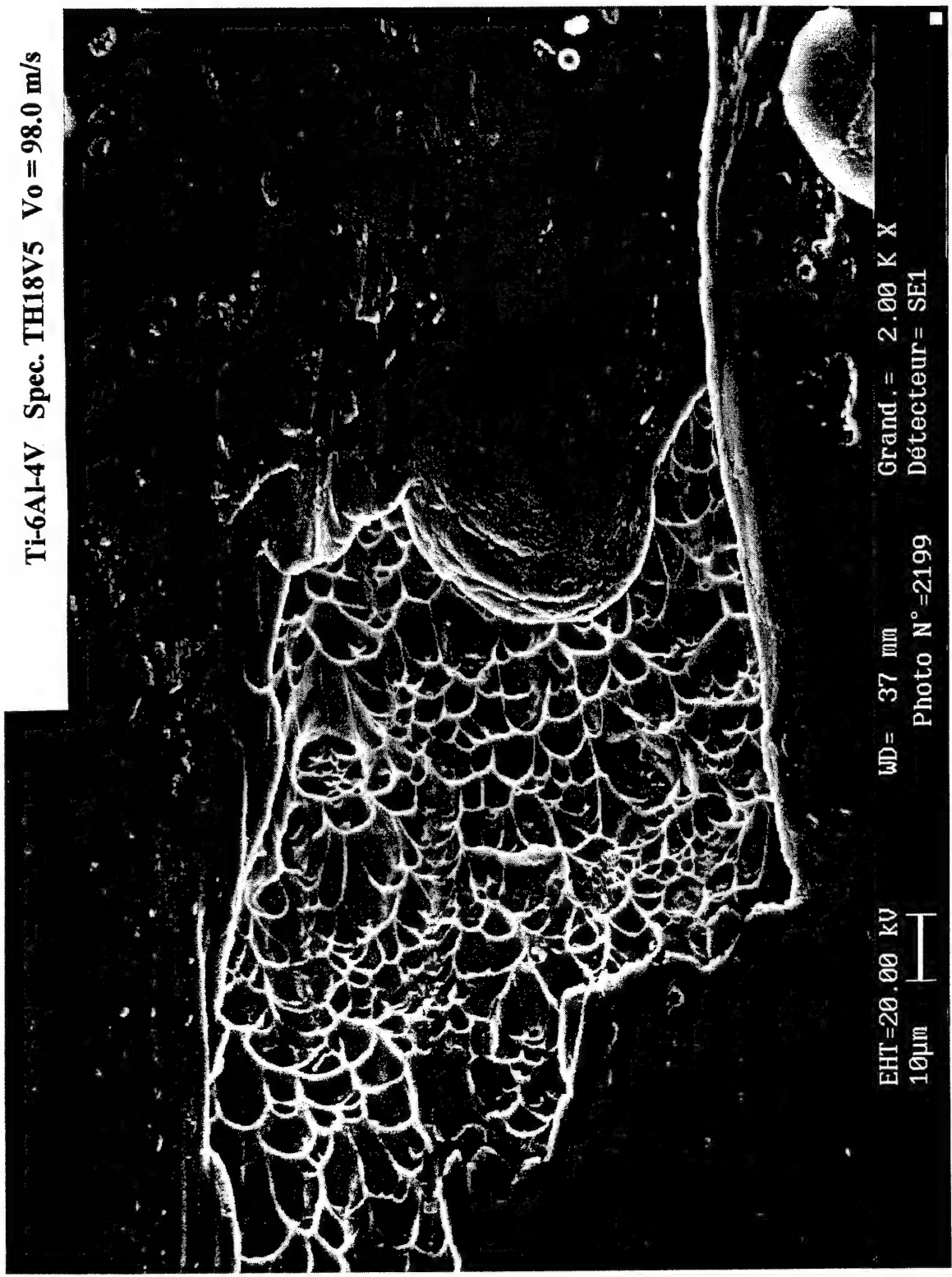
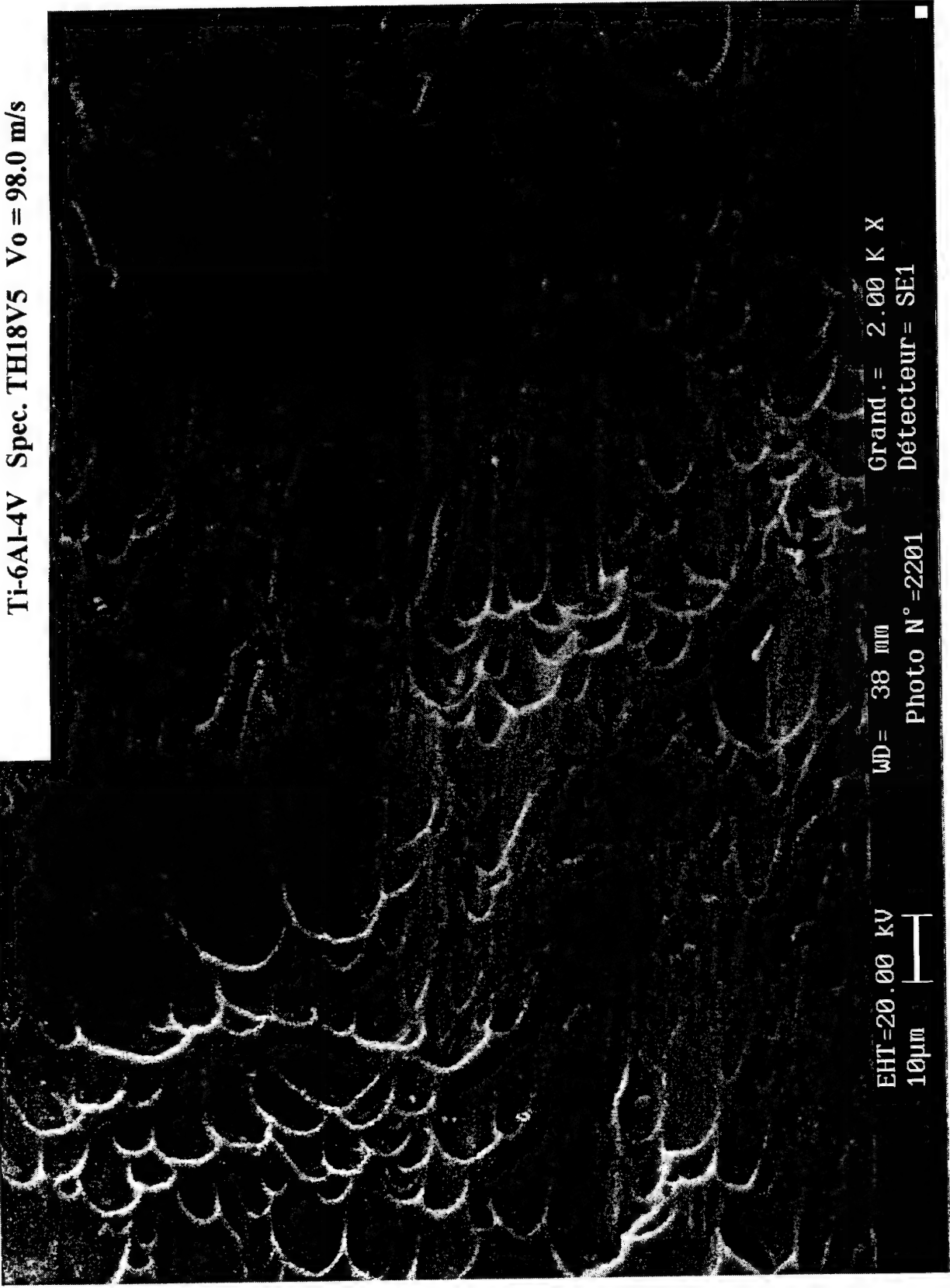


Fig. 31

Ti-6Al-4V Spec. TH18V5 $V_0 = 98.0 \text{ m/s}$



EHT=20.00 KV
WD= 38 mm
Photo N°=2201
Grand.= 2.00 K X
DéTECTeur= SE1
10 μm

Fig. 32

Ti-6Al-4V Spec. TH31V6 $V_0 = 107.4 \text{ m/s}$

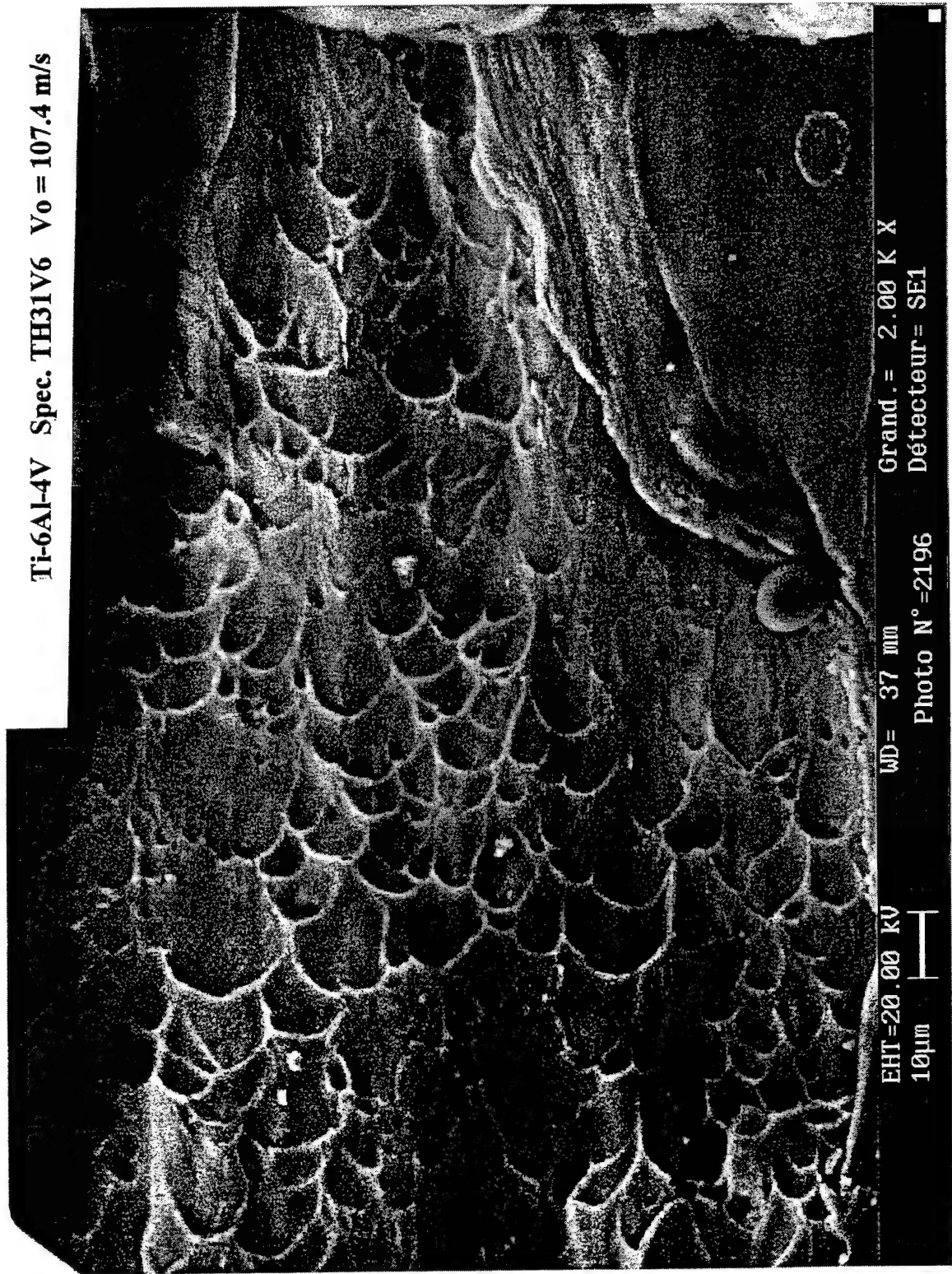


Fig. 33

Ti-6Al-4V Spec. TH31V6 $V_0 = 107.4 \text{ m/s}$

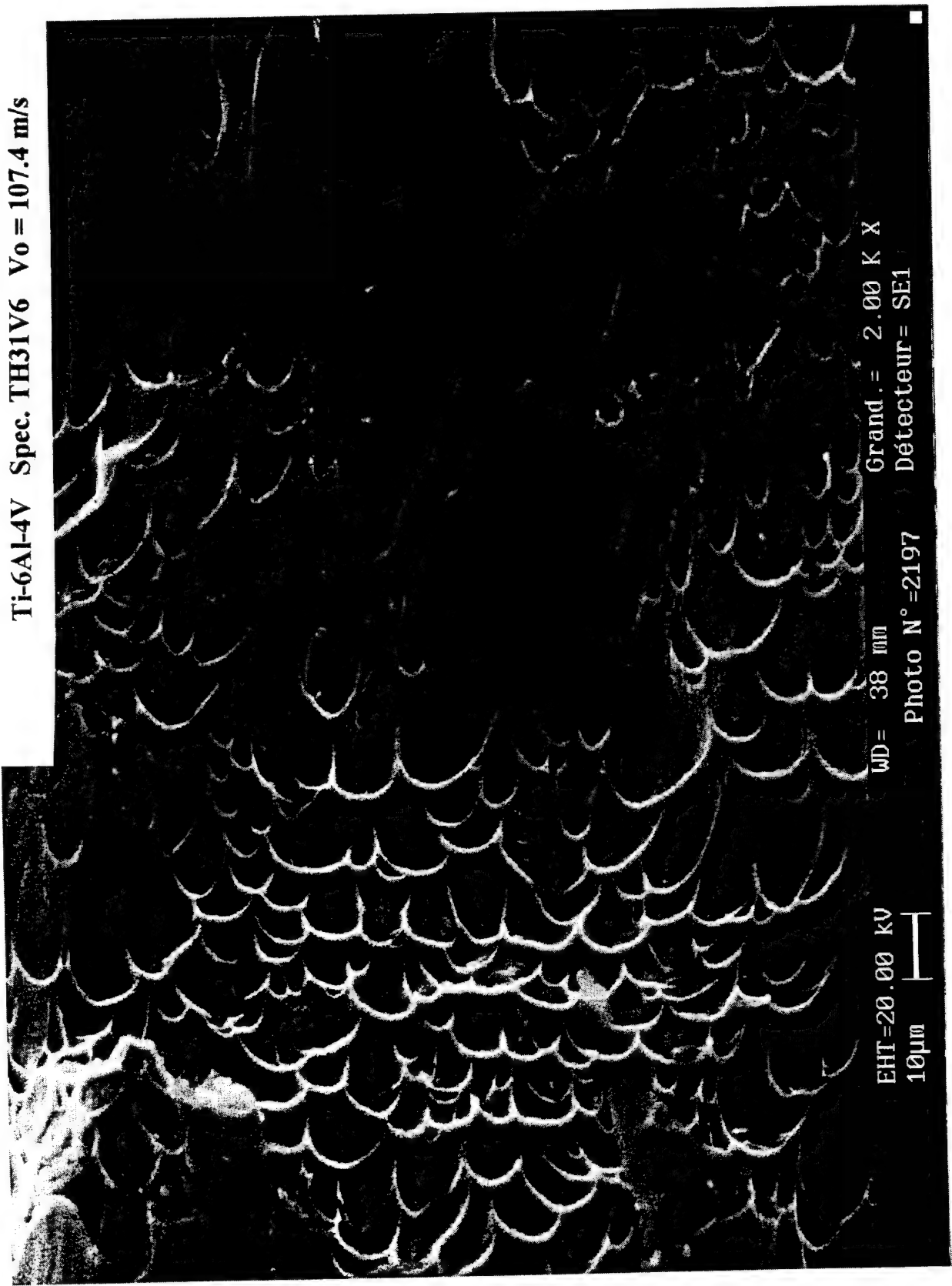
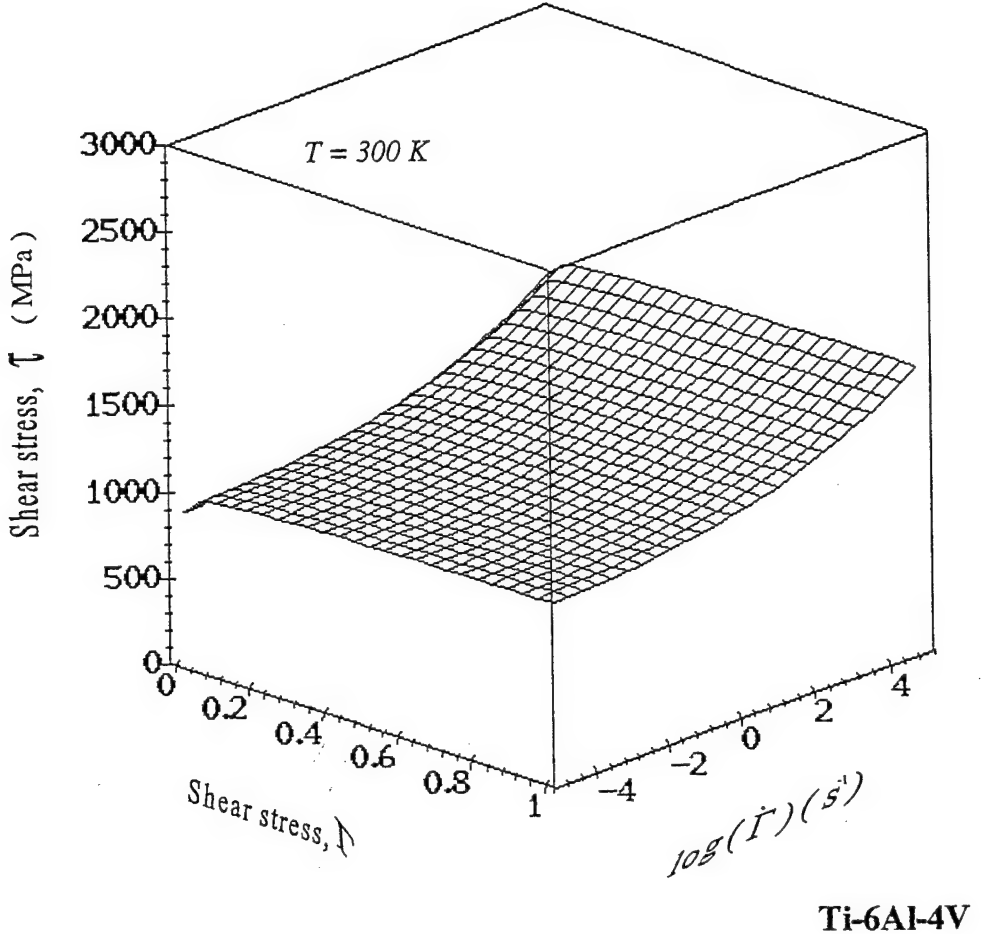


Fig. 34



Ti-6Al-4V

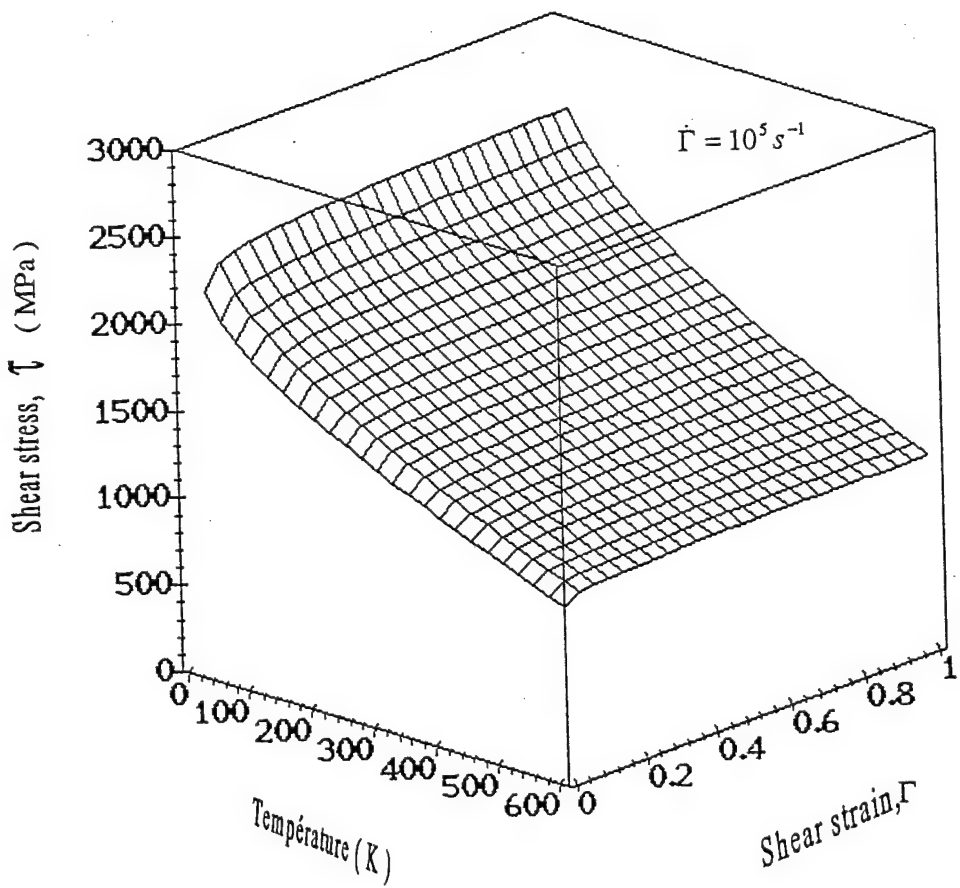


Fig. 35

Ti-6Al-4V

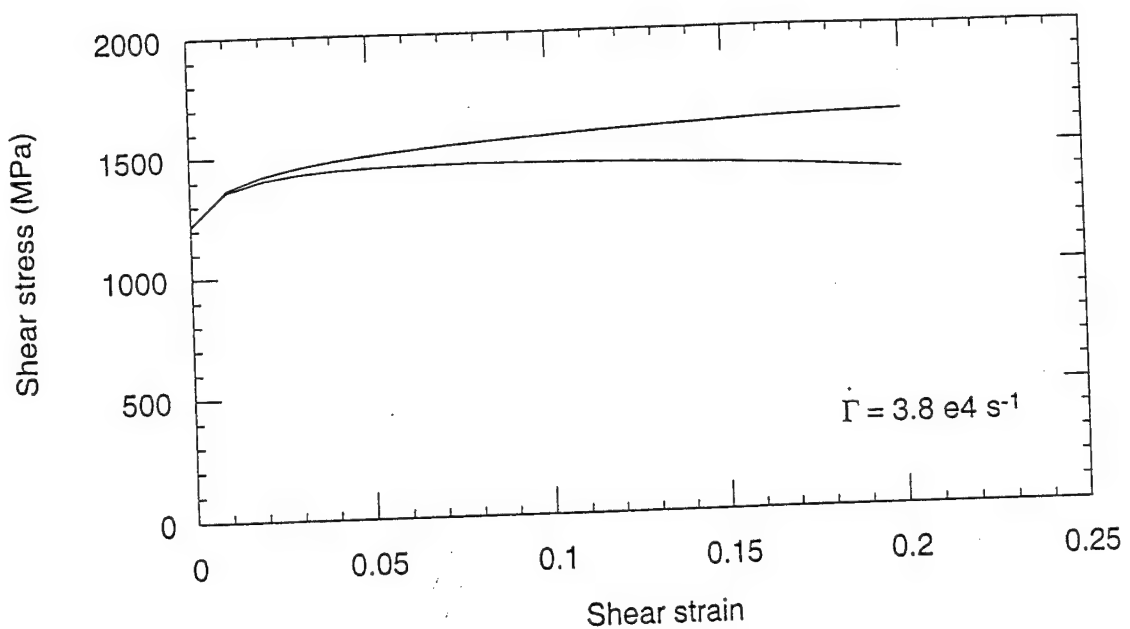


Fig. 36

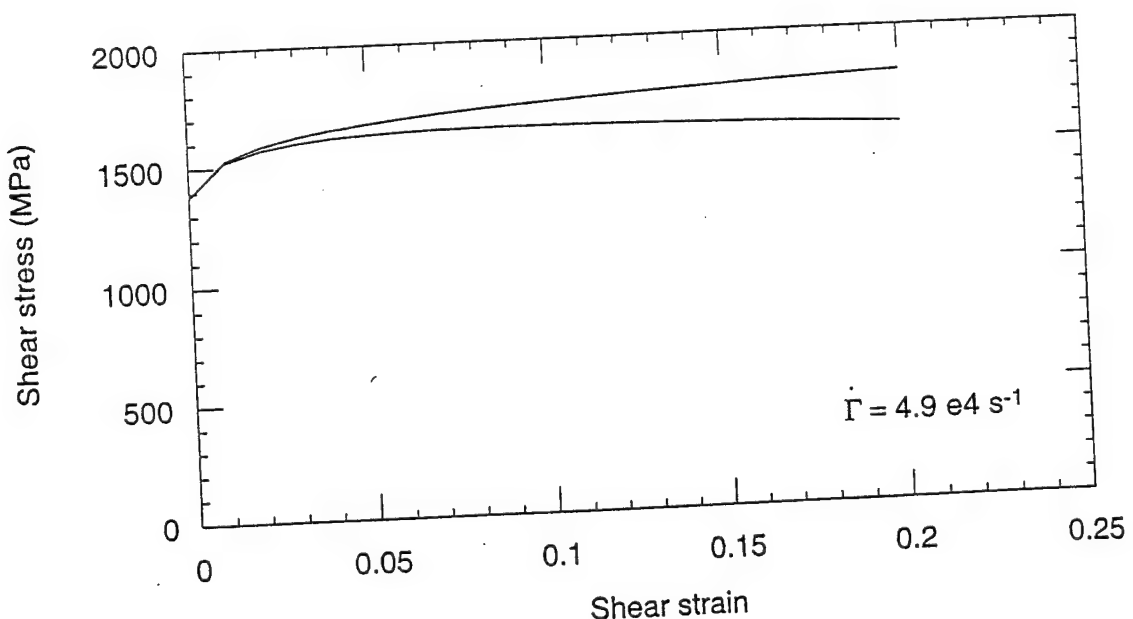


Fig. 37

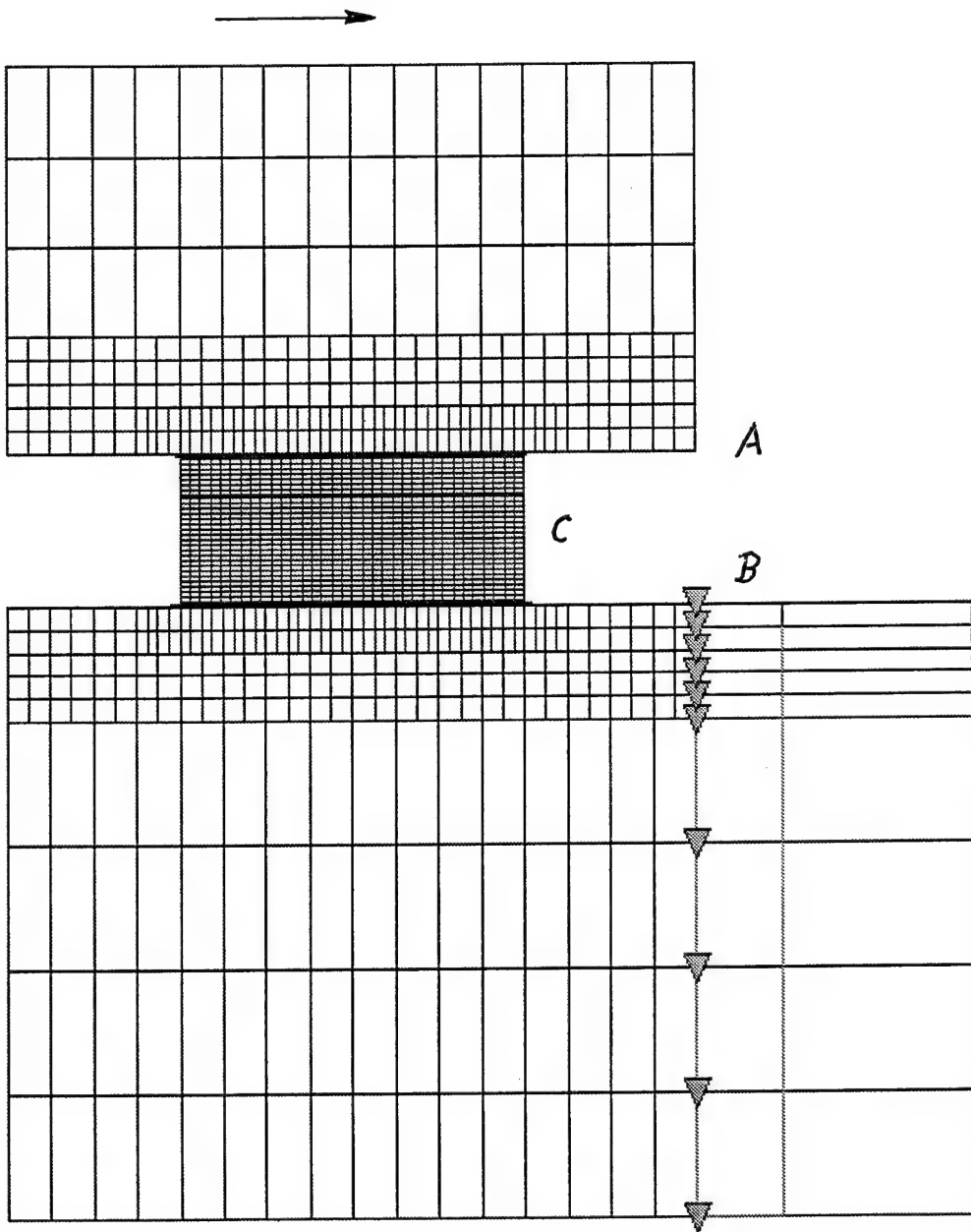


Fig. 38

Ti-6Al-4V ALLOY

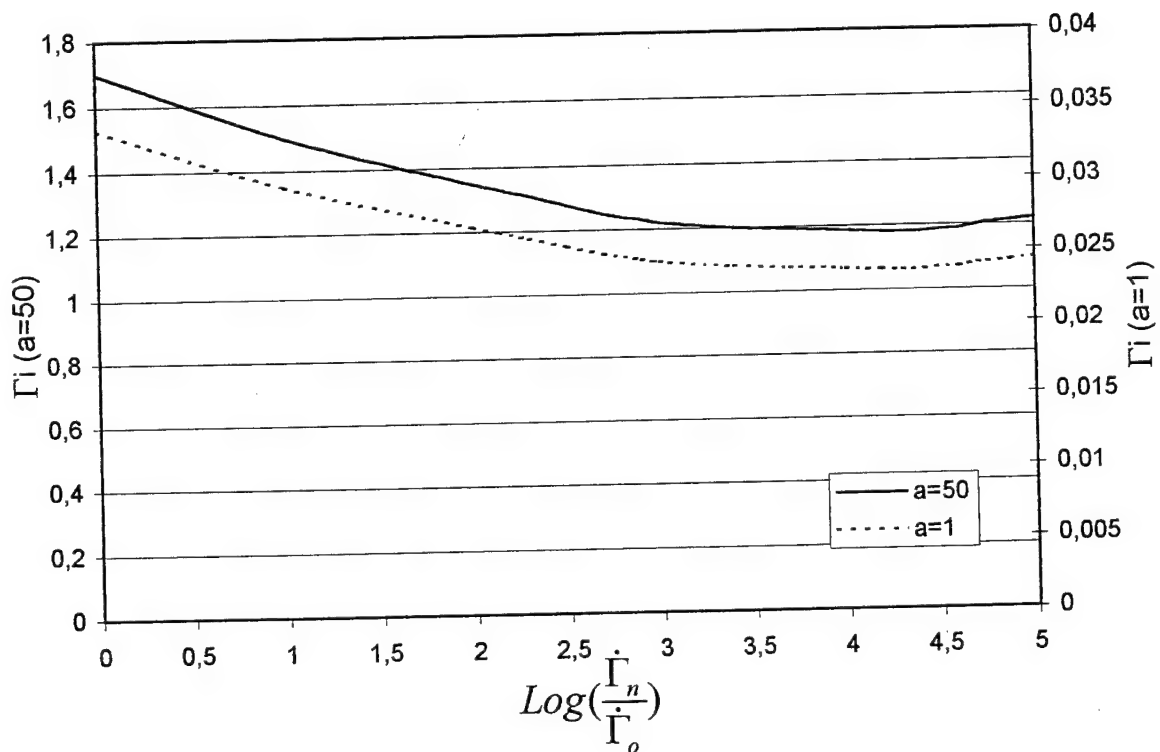


Fig. 39

$V=100\text{m/s}$

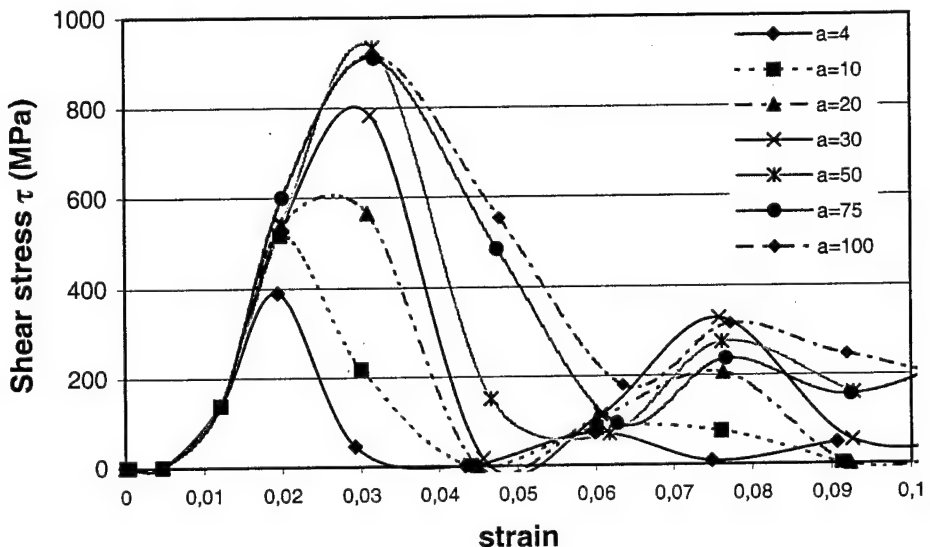


Fig. 40

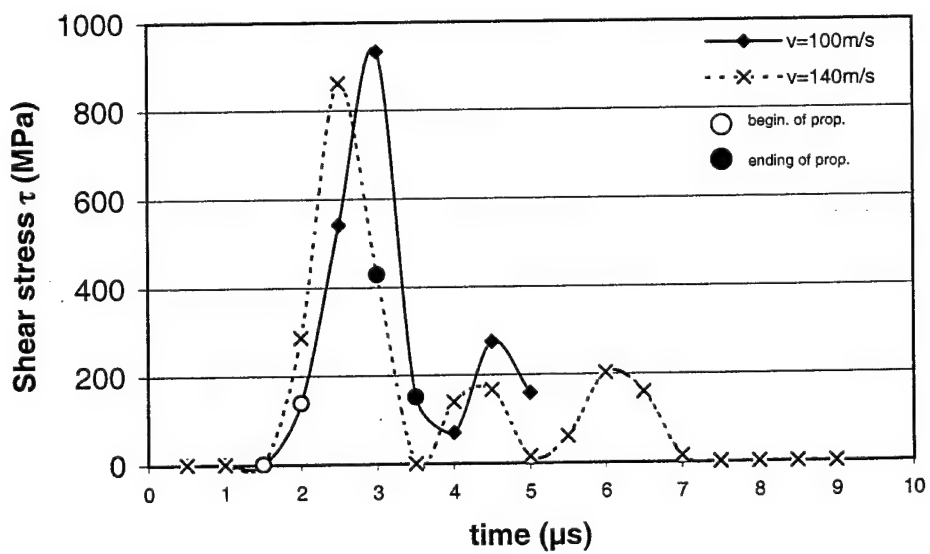


Fig. 41

$$v_0 = 20 \text{ m/s} \quad \Gamma_n^{\circ} = 1 \cdot 10^4 \text{ s}^{-1}$$

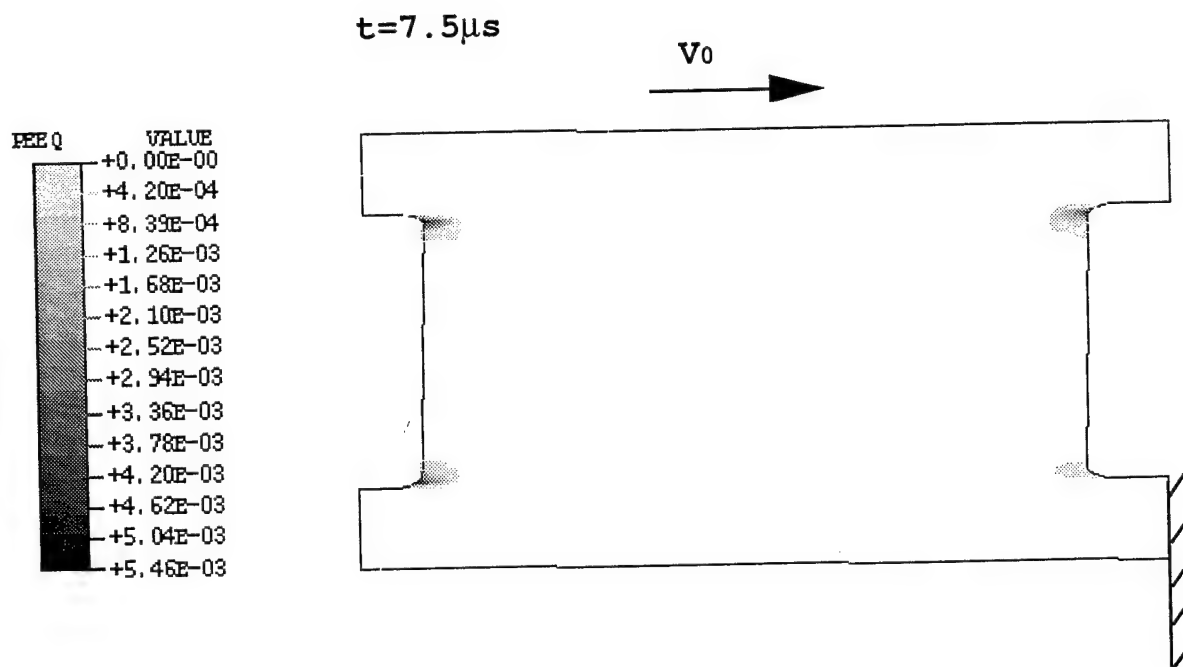


Fig. 42

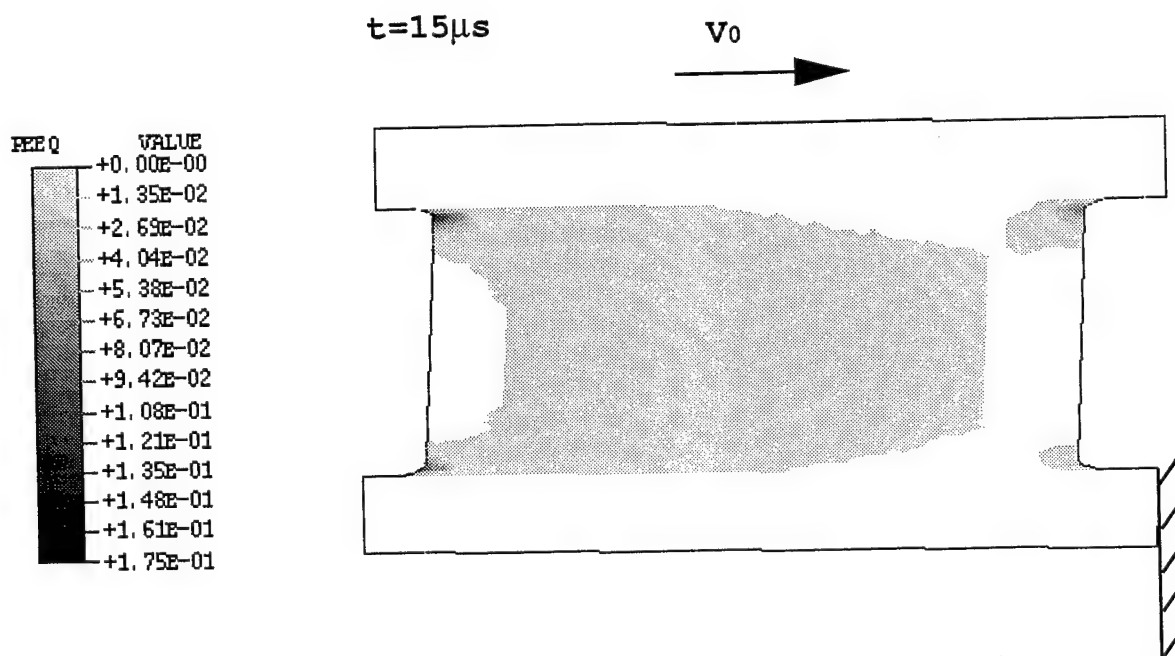


Fig. 43

$$V_0 = 100 \text{ m/s} \quad \Gamma_n = 5 \times 10^4 \text{ s}^{-1}$$

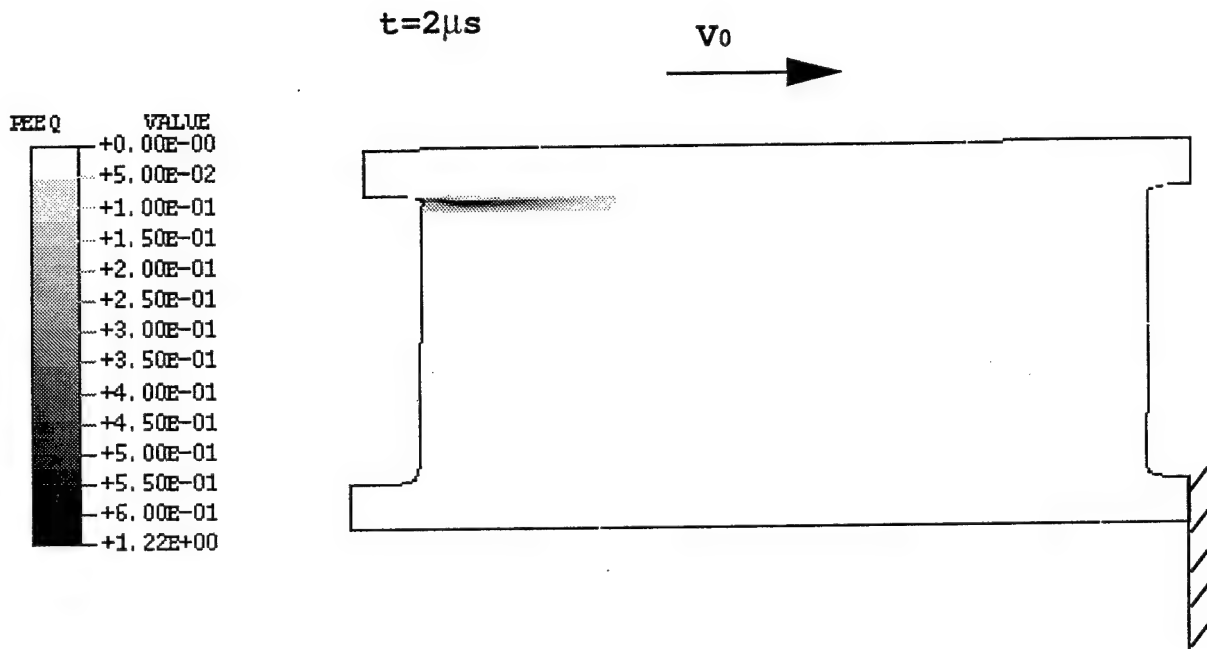


Fig. 44

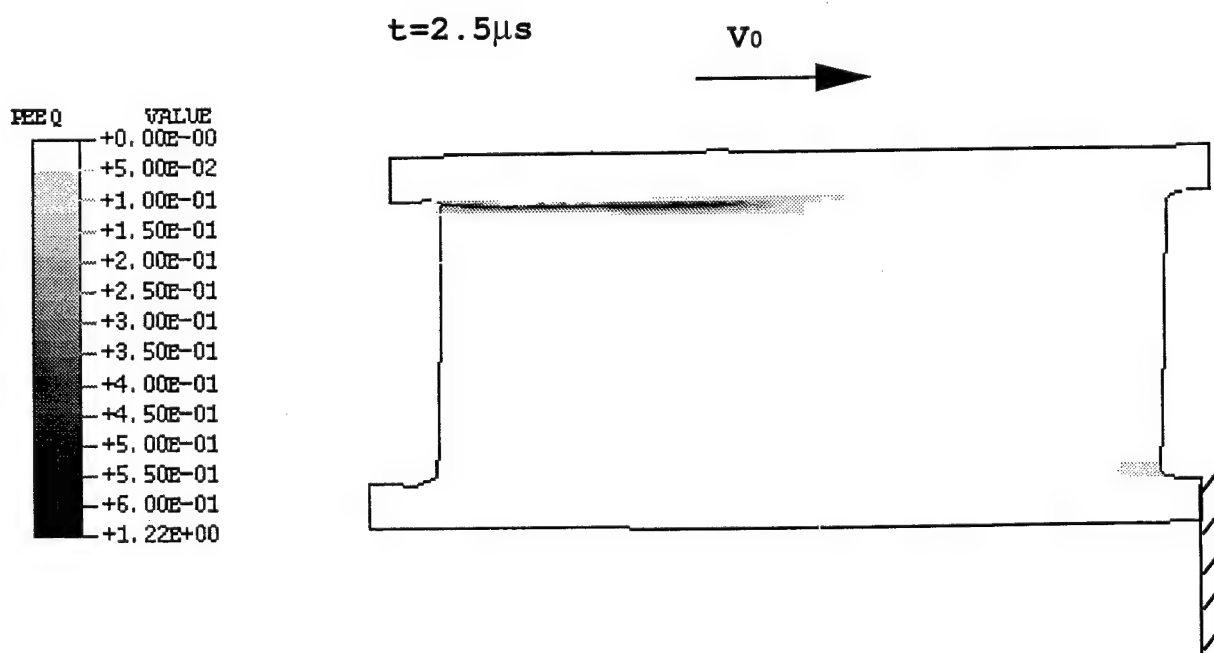


Fig. 45

$$V_0 = 20 \text{ m/s} \quad \Gamma_n = 1 \cdot 10^4 \text{ s}^{-1}$$

$t = 22.5 \mu\text{s}$

V_0

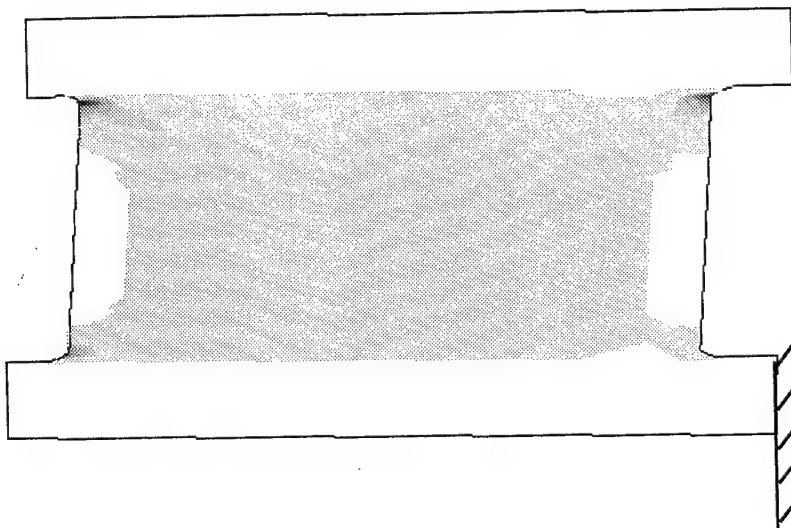
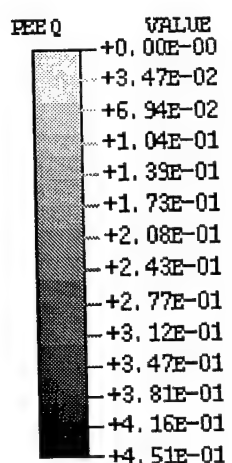


Fig. 46

$t = 30 \mu\text{s}$

V_0

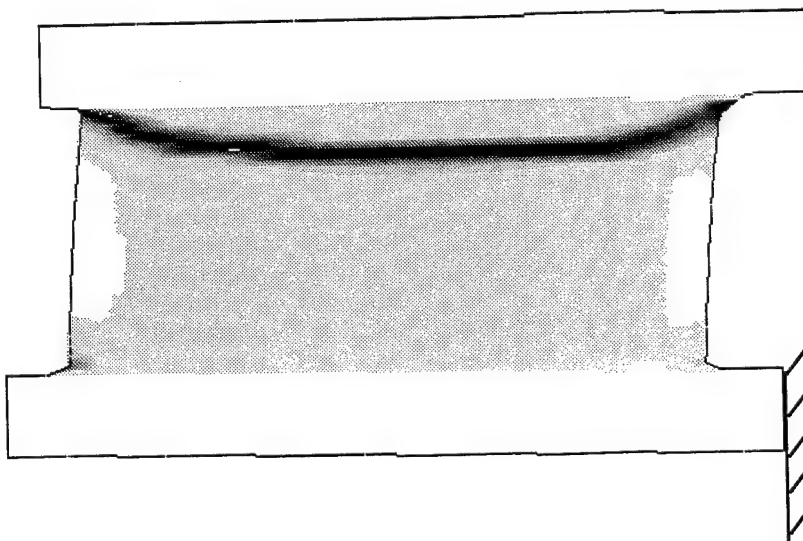
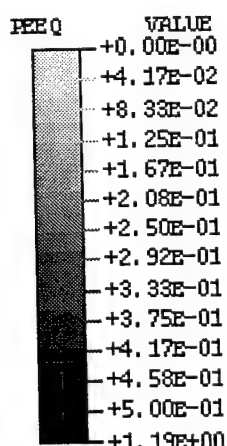


Fig. 47

$$V_0 = 100 \text{ m/s}$$

$$\Gamma_n = 5 \times 10^4 \text{ s}^{-1}$$

$t = 3 \mu\text{s}$

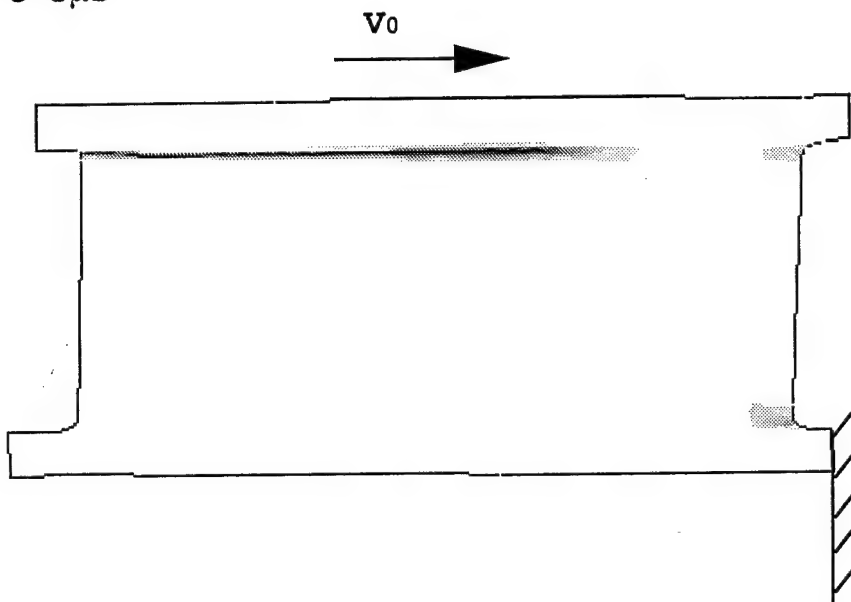
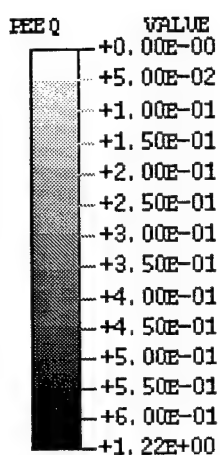


Fig. 48

$t = 3.5 \mu\text{s}$

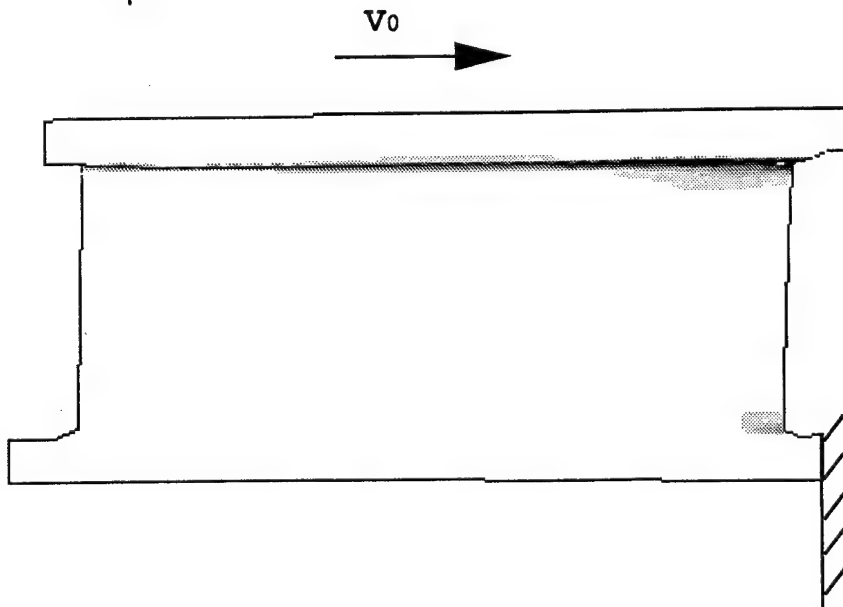
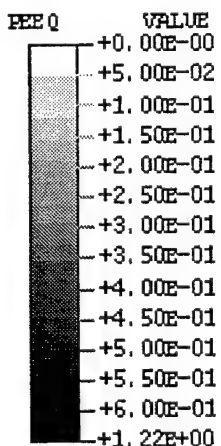


Fig. 49

rise time=1 μ s

Ti-6Al-4V

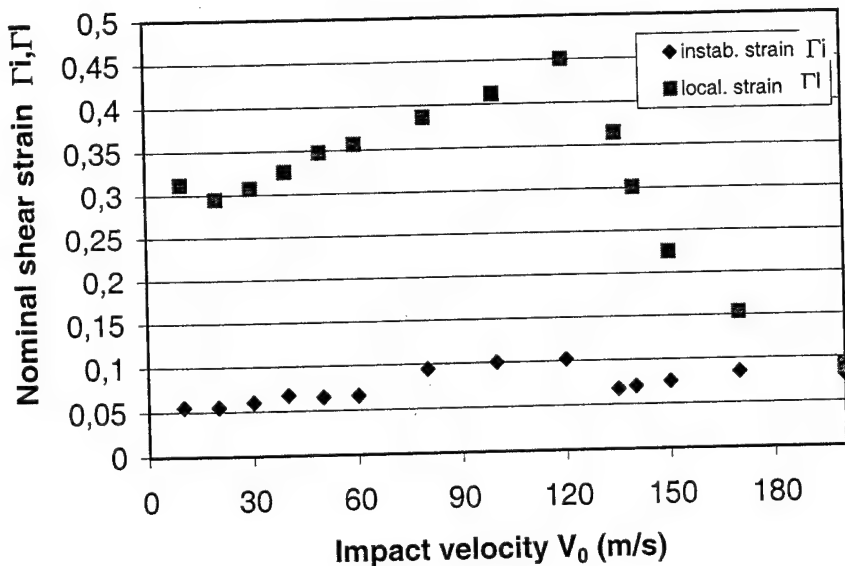


Fig. 50

Ti-6Al-4V

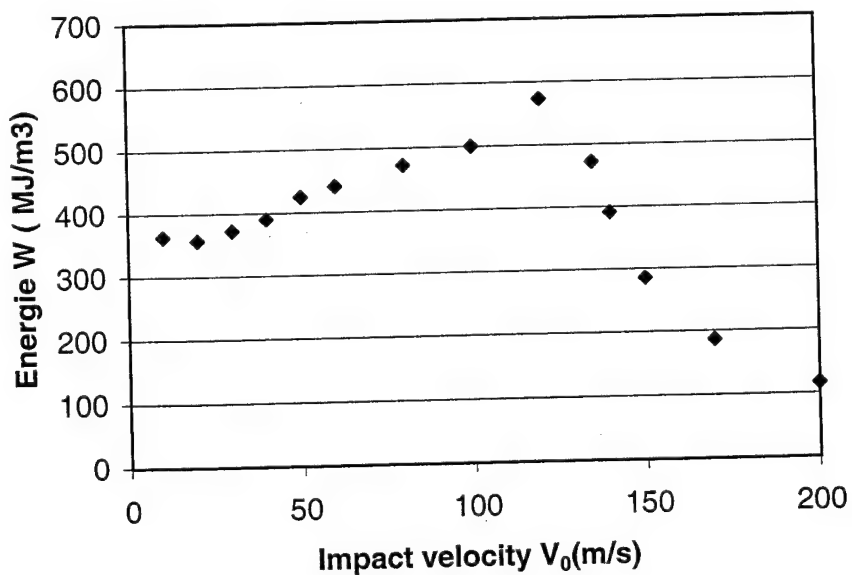


Fig. 51

rise time=0.1 μ s

Ti-6Al-4V

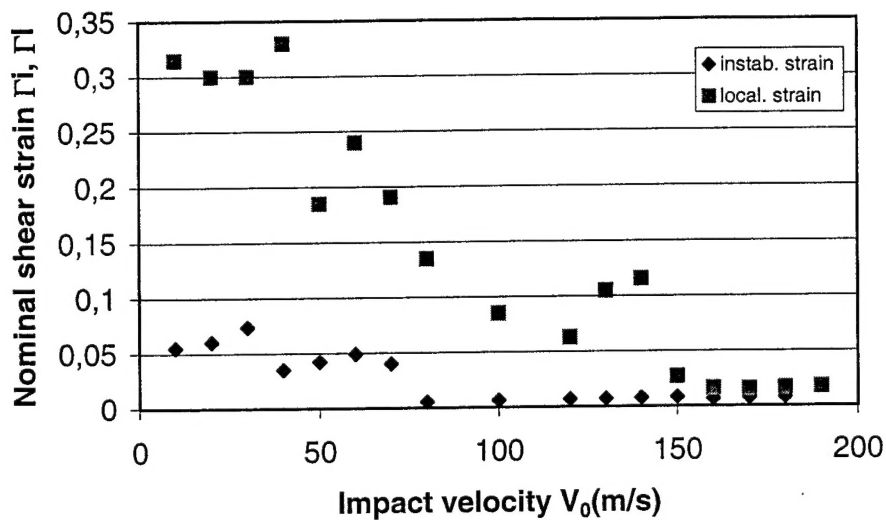


Fig. 52

Ti-6Al-4V

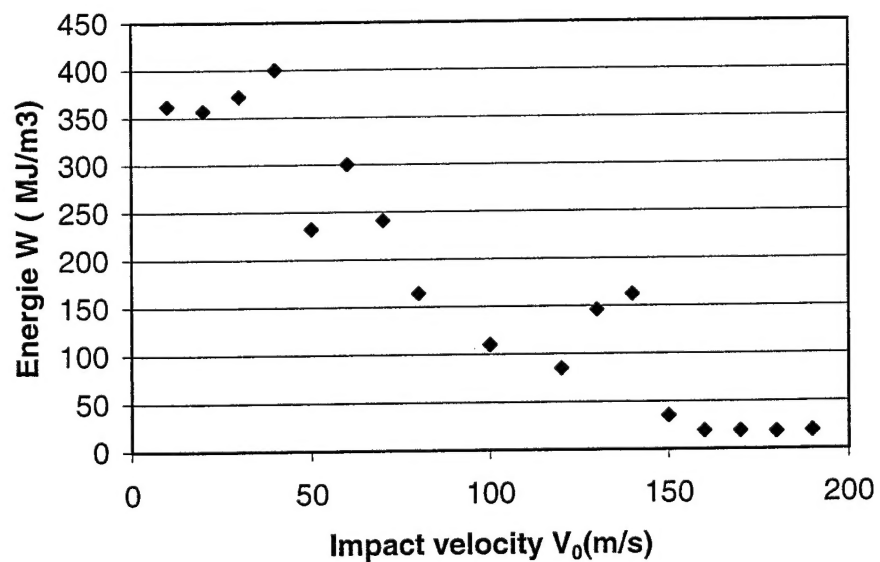


Fig. 53

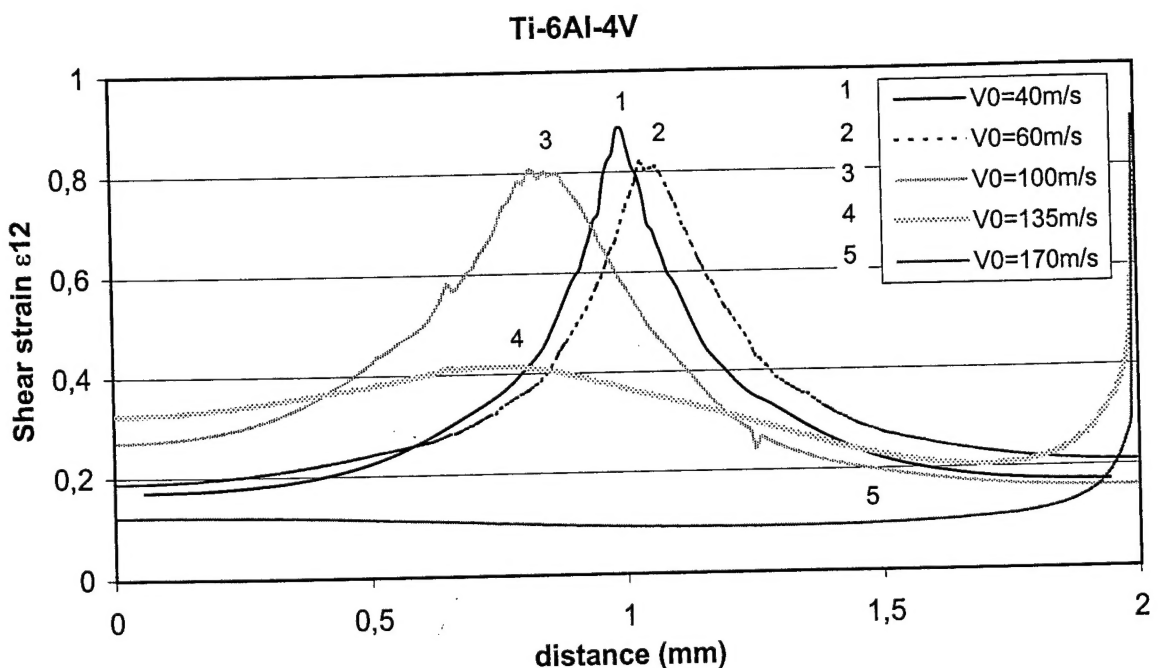


Fig. 54

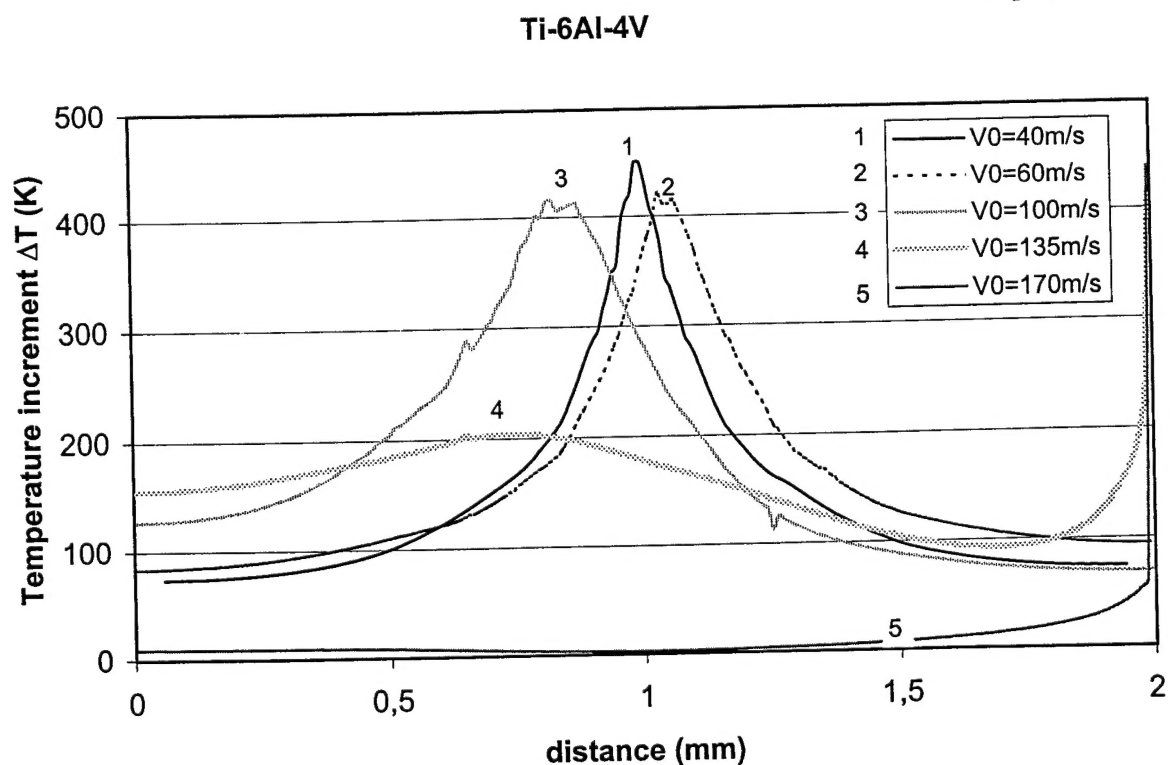


Fig. 55

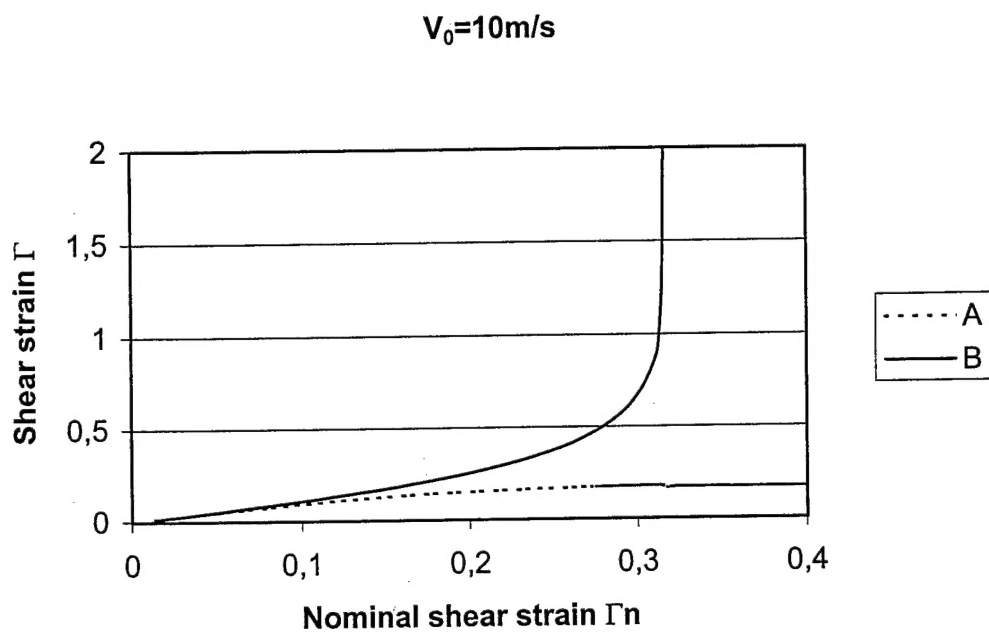
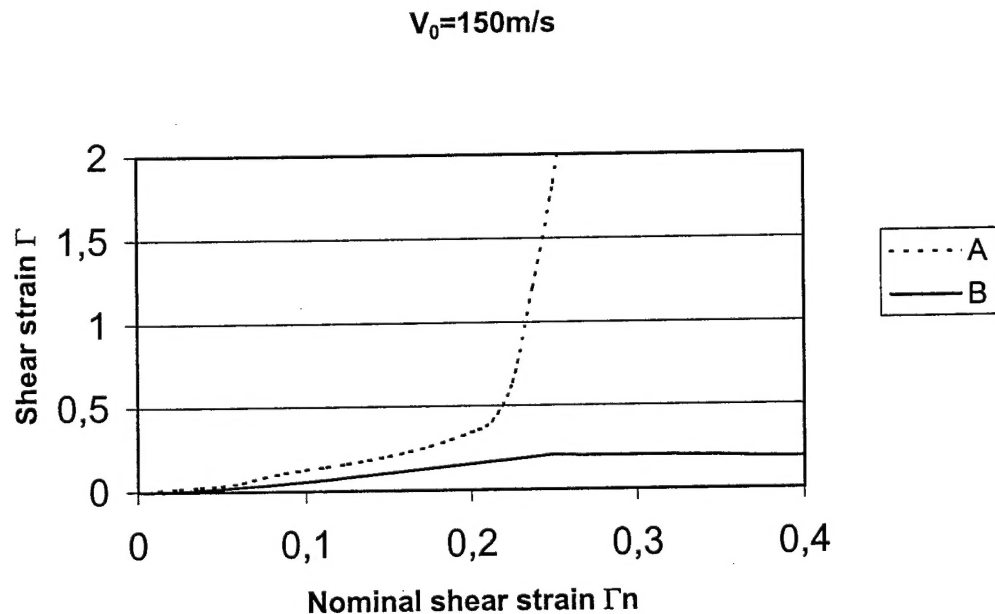


Fig. 56



Ti-6Al-4V

Fig. 57

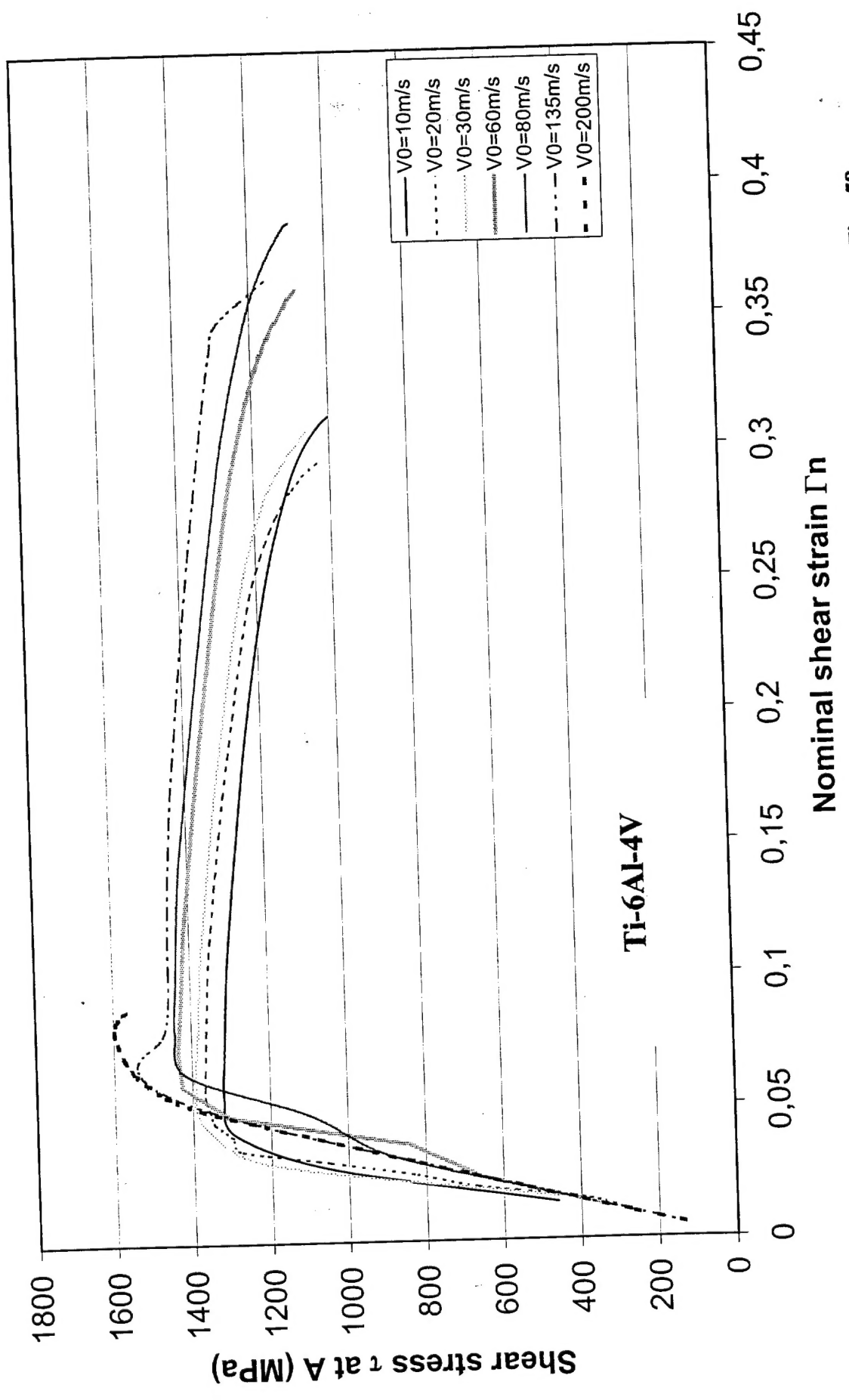


Fig. 58